

# Predictive power of polynomial machine learning potentials for liquid states in 22 elemental systems

Hayato Wakai,<sup>\*</sup> Atsuto Seko,<sup>†</sup> Hirosato Izuta, Takayuki Nishiyama, and Isao Tanaka  
*Department of Materials Science and Engineering, Kyoto University, Kyoto 606-8501, Japan*  
(Dated: June 12, 2024)

The polynomial machine learning potentials (MLPs) described by polynomial rotational invariants have been systematically developed for various systems and used in diverse applications in crystalline states. In this study, we systematically investigate the predictive power of the polynomial MLPs for liquid structural properties in 22 elemental systems with diverse chemical bonding properties, including those showing anomalous melting behavior, such as Si, Ge, and Bi. We compare liquid structural properties obtained from molecular dynamics simulations using the density functional theory (DFT) calculation, the polynomial MLPs, and other interatomic potentials in the literature. The current results demonstrate that the polynomial MLPs consistently exhibit high predictive power for liquid structural properties with the same accuracy as that of typical DFT calculations.

## I. INTRODUCTION

Molecular dynamics (MD) simulations are powerful tools for performing atomistic simulations in a wide range of applications. For MD simulations in liquid and liquid-like disordered states, empirical interatomic potentials such as pair potentials (e.g., Lennard–Jones (LJ) potential [1]), embedded atom method (EAM) potentials [2], and Stillinger–Weber (SW) potentials [3] have been commonly employed [4–7]. Although the empirical interatomic potentials allow us to extend the simulation time and the number of atoms in the simulation cell significantly, their simplistic models often restrict their application and target system, as will also be demonstrated in this study. *Ab initio* MD (AIMD) can be an alternative way to perform accurate atomistic simulations [8, 9]. However, its high computational cost limits its application.

Machine learning potentials (MLPs) [10–29] have been in increased demand for accurate and efficient large-scale simulations that are prohibitively expensive using the density functional theory (DFT) calculation. The MLPs represent interatomic interactions with systematic structural features and flexible machine learning models such as artificial neural networks, Gaussian process models, and linear models. Because the MLPs are typically developed from extensive DFT datasets, they should have high predictive power for structures close to those in the datasets. They have been applied to efficient and accurate calculations for liquid states [18, 30, 31].

The polynomial MLP is an approach to develop MLPs that are accurate for a wide variety of structures [32–34]. The polynomial MLP is described as polynomial rotational invariants systematically derived from order parameters in terms of radial and spherical harmonic functions. Because simple polynomial functions are employed instead of artificial neural networks and Gaussian process

models, the descriptive power for the potential energy is strongly dependent on their polynomial forms. At the same time, efficient model estimations can be achieved using linear regressions supported by powerful libraries for linear algebra [34]. Moreover, the force and stress tensor components in DFT training datasets can be considered in a straightforward manner [34]. Even when considering the force and stress tensor components as training data entries, it is possible to estimate model coefficients efficiently using fast linear regressions.

Following these advantages, polynomial MLPs have been systematically developed for various systems. Various developed polynomial MLPs with different trade-offs between accuracy and computational efficiency are available in the Polynomial Machine Learning Potential Repository [35]. Currently, the repository contains MLPs for 48 elemental and 120 binary alloy systems. They have been used for applications in crystalline states [32, 33, 36, 37], which indicates that they can enable us to predict properties accurately for various crystal structures. In this study, we systematically investigate the predictive power of polynomial MLPs for liquid states in 22 elemental systems, i.e., Li, Be, Na, Mg, Al, Si, Ti, V, Cr, Cu, Zn, Ga, Ge, Ag, Cd, In, Sn, Au, Hg, Tl, Pb, and Bi. We compare the structural quantities commonly used to describe liquid structures computed using the DFT calculations, the polynomial MLPs, and other interatomic potentials. The current targets include elemental systems known to exhibit anomalous melting behavior, such as Si, Ge, Sn, Ga, and Bi [38–40]. As will be shown below, complex descriptions for the potential energy using the MLPs are essential for accurately predicting liquid structural quantities.

## II. METHODOLOGY

### A. Polynomial machine learning potentials

In this section, we present the formulation of the polynomial MLP in elemental systems, which can be sim-

<sup>\*</sup> wakai@cms.mtl.kyoto-u.ac.jp

<sup>†</sup> seko@cms.mtl.kyoto-u.ac.jp

plified from the formulation for multicomponent systems [33, 34]. The short-range part of the potential energy for a structure,  $E$ , is assumed to be decomposed as  $E = \sum_i E^{(i)}$ , where  $E^{(i)}$  denotes the contribution of interactions between atom  $i$  and its neighboring atoms within a given cutoff radius  $r_c$ , referred to as the atomic energy. The atomic energy is then approximately given by a function of invariants  $\{d_m^{(i)}\}$  with any rotations centered at the position of atom  $i$  as

$$E^{(i)} = F\left(d_1^{(i)}, d_2^{(i)}, \dots\right), \quad (1)$$

$$d_{nl_1 l_2 \dots l_p, (\sigma)}^{(i)} = \sum_{m_1, m_2, \dots, m_p} c_{m_1 m_2 \dots m_p}^{l_1 l_2 \dots l_p, (\sigma)} a_{nl_1 m_1}^{(i)} a_{nl_2 m_2}^{(i)} \dots a_{nl_p m_p}^{(i)}, \quad (2)$$

where the order parameter  $a_{nlm}^{(i)}$  is component  $nlm$  of the neighboring atomic density of atom  $i$ . The coefficient set  $\{c_{m_1 m_2 \dots m_p}^{l_1 l_2 \dots l_p, (\sigma)}\}$  ensures that the linear combinations are invariant for arbitrary rotations, which can be enumerated using group theoretical approaches such as the projection operator method [32, 41]. In terms of fourth- and higher-order polynomial invariants, multiple linear combinations are linearly independent for most of the set  $\{l_1, l_2, \dots, l_p\}$ . They are distinguished by index  $\sigma$  if necessary.

Here, the radial functions are Gaussian-type ones expressed by

$$f_n(r) = \exp[-\beta_n(r - r_n)^2] f_c(r), \quad (3)$$

where  $\beta_n$  and  $r_n$  denote given parameters. The cutoff function  $f_c$  ensures the smooth decay of the radial function. The current MLP employs a cosine-based cutoff function expressed as

$$f_c(r) = \begin{cases} \frac{1}{2} \left[ \cos\left(\pi \frac{r}{r_c}\right) + 1 \right] & (r \leq r_c) \\ 0 & (r > r_c) \end{cases}. \quad (4)$$

The order parameter of atom  $i$ ,  $a_{nlm}^{(i)}$ , is approximately evaluated from the neighboring atomic distribution of atom  $i$  as

$$a_{nlm}^{(i)} = \sum_{\{j|r_{ij} \leq r_c\}} f_n(r_{ij}) Y_{lm}^*(\theta_{ij}, \phi_{ij}), \quad (5)$$

where  $(r_{ij}, \theta_{ij}, \phi_{ij})$  denotes the spherical coordinates of neighboring atom  $j$  centered at the position of atom  $i$ . Note that this approximation for the order parameters ignores the nonorthonormality of the Gaussian-type radial functions, but it is acceptable in developing the polynomial MLP [32].

Given a set of structural features  $D^{(i)} = \{d_1^{(i)}, d_2^{(i)}, \dots\}$ , the polynomial function  $F_\xi$  composed of all combinations of  $\xi$  structural features is

where  $d_m^{(i)}$  can be referred to as a structural feature for modeling the potential energy. The polynomial MLP adopts polynomial invariants of the order parameters representing the neighboring atomic density as structural features and employs polynomial functions as function  $F$ .

When the neighboring atomic density is described by radial functions  $\{f_n\}$  and spherical harmonics  $\{Y_{lm}\}$ , a  $p$ th-order polynomial invariant for radial index  $n$  and set of angular numbers  $\{l_1, l_2, \dots, l_p\}$  is given by a linear combination of products of  $p$  order parameters, expressed as

represented as

$$\begin{aligned} F_1(D^{(i)}) &= \sum_s w_s d_s^{(i)}, \\ F_2(D^{(i)}) &= \sum_{\{st\}} w_{st} d_s^{(i)} d_t^{(i)}, \\ F_3(D^{(i)}) &= \sum_{\{stu\}} w_{stu} d_s^{(i)} d_t^{(i)} d_u^{(i)}, \end{aligned} \quad (6)$$

where  $w$  denotes a regression coefficient. A polynomial of the polynomial invariants  $D^{(i)}$  is then described as

$$E^{(i)} = F_1(D^{(i)}) + F_2(D^{(i)}) + F_3(D^{(i)}) + \dots \quad (7)$$

The current models have no constant terms, which means that the atomic energy is measured from the energies of isolated atoms. In addition to the model given by Eq. (7), simpler models composed of a linear polynomial of structural features and a polynomial of a subset of the structural features are also introduced, such as

$$E^{(i)} = F_1(D^{(i)}) + F_2(D_{\text{pair}}^{(i)} \cup D_2^{(i)}), \quad (8)$$

where subsets of  $D^{(i)}$  are denoted by

$$D_{\text{pair}}^{(i)} = \{d_{n0}^{(i)}\}, D_2^{(i)} = \{d_{nll}^{(i)}\}. \quad (9)$$

Note that the polynomial MLP is equivalent to a spectral neighbor analysis potential (SNAP) [24] when the linear polynomial model with up to third-order invariants is expressed as

$$E^{(i)} = F_1(D_{\text{pair}}^{(i)} \cup D_2^{(i)} \cup D_3^{(i)}), \quad (10)$$

where subset  $D_3^{(i)}$  is given as  $D_3^{(i)} = \{d_{nl_1 l_2 l_3}^{(i)}\}$ . Similarly, the current formulation includes a quadratic SNAP [25], which is an extension of the SNAP. In addition, linear

polynomial models using polynomial invariants are analogous to the formulation of the atomic cluster expansion [42].

Each of the polynomial MLPs was created from a training dataset using PYPOLYMLP [34, 43], and its prediction errors for the energy, force components, and stress tensors were estimated using a test dataset. The training and test datasets for each elemental metal were generated as follows. First, we fully optimized the atomic positions and lattice constants of 86 prototype structures [32] using the DFT calculation. They comprise single elements with the zero oxidation state from the Inorganic Crystal Structure Database (ICSD) [44], including metallic closed-packed structures, covalent structures, layered structures, and structures reported as high-pressure phases. Then, 13000–15000 structures were generated from the optimized prototype structures, and they were randomly divided into training and test datasets at a ratio of nine to one. Each structure was constructed by randomly introducing lattice expansions, lattice distortions, and atomic displacements into a supercell of an optimized prototype structure. No structural data in liquid states, such as structural trajectories in MD simulations at high temperatures, were used to develop the polynomial MLPs.

Non-spin-polarized DFT calculations were performed for structures in the datasets using the plane-wave-basis projector augmented wave (PAW) method [45, 46] within the Perdew–Burke–Ernzerhof (PBE) exchange-correlation functional [47], as implemented in the VASP code [8, 48, 49]. The cutoff energy was set to 300 eV. The total energies converged to less than  $10^{-3}$  meV/supercell. The allowed spacing between  $k$ -points was approximately set to  $0.09 \text{ \AA}^{-1}$ . The atomic positions and lattice constants of the prototype structures were optimized until the residual forces were less than  $10^{-2}$  eV/Å. The PAW potentials used in DFT calculations are listed in Appendix A, and these PAW potentials include scalar-relativistic corrections. Spin-orbit coupling was not considered in all the elemental systems.

Regression coefficients of potential energy models were estimated using linear ridge regression. The energy values and force components in the training dataset were used as observations in the regression. The ridge regularization parameter was optimized to minimize the prediction error for the test dataset.

The accuracy and computational efficiency of the polynomial MLP greatly depend on the input parameters, such as the cutoff radius and the number of order parameters. Therefore, a systematic grid search was conducted to find their optimal values in each system. As indicated in Ref. [32], the accuracy and computational efficiency are conflicting properties, hence, a set of Pareto-optimal MLPs with different trade-offs between the accuracy and computational efficiency was obtained from the grid search.

Figure 1 shows the distribution of the energies of structures in the training and test datasets computed using the

DFT calculation and those calculated using the polynomial MLP, which has the lowest prediction error. The polynomial MLP reveals a narrow distribution of errors. Figure 2 shows the absolute prediction errors of the cohesive energy for various prototype structures. The polynomial MLP exhibits minor errors for almost all prototype structures. These results indicate that the polynomial MLP is accurate for many typical structures and their derivatives containing diverse neighborhood environments and coordination numbers.

## B. Computational procedures for MD simulations

Multiple Pareto-optimal MLPs developed using the above procedure are available in the repository [34, 35]. They show different trade-offs between accuracy and computational efficiency. Although a polynomial MLP is generally chosen from the set of Pareto-optimal MLPs for performing atomistic simulations, we examine the accuracy of all Pareto-optimal MLPs for liquid states.

We perform MD simulations using the polynomial MLPs and the DFT calculation for elemental Li, Be, Na, Mg, Al, Si, Ti, V, Cr, Cu, Zn, Ga, Ge, Ag, Cd, In, Sn, Au, Hg, Tl, Pb, and Bi at temperatures close to and above their melting temperatures. We also employ empirical interatomic potentials and other MLPs available in open repositories such as OpenKim [50] and the interatomic potential repository [51].

The MD simulations were performed within the NVT ensemble, employing the Nose–Hoover thermostat [52, 53] to control the temperature. MD simulations were carried out using the LAMMPS code [54]. The current computational procedure for performing a single MD simulation is as follows. We first generate a cubic periodic cell with 125 atoms arranged on a  $5 \times 5 \times 5$  regular grid. The cell volume is given such that the cell density corresponds to the experimental density at its melting temperature, as reported in Ref. [55]. The cell density for the elemental Hg is exceptionally given as  $12.4 \text{ g/cm}^3$ . This cell density value was employed by Kresse and Hafner [56]. The atomic configurations are then equilibrated using MD run for 3 ps at a temperature typically 700 K higher than the experimental melting temperature to obtain a snapshot in the liquid state. The MD time step is set to 3 fs. The atomic configurations are further equilibrated from the snapshot structure using MD run for at least 3 ps at the target temperature. Finally, we perform MD run for 15 ps at the target temperature and calculate structural quantities as ensemble averages over the MD trajectory.

For the AIMD simulations, non-spin-polarized DFT calculations were performed using the plane-wave-basis PAW method [45, 46] within the PBE exchange-correlation functional [47], as implemented in the VASP code [8, 48, 49]. The cutoff energy was set to 400 eV. The integration in the reciprocal space was performed at the  $\Gamma$ -point only. The PAW potentials listed in Ap-

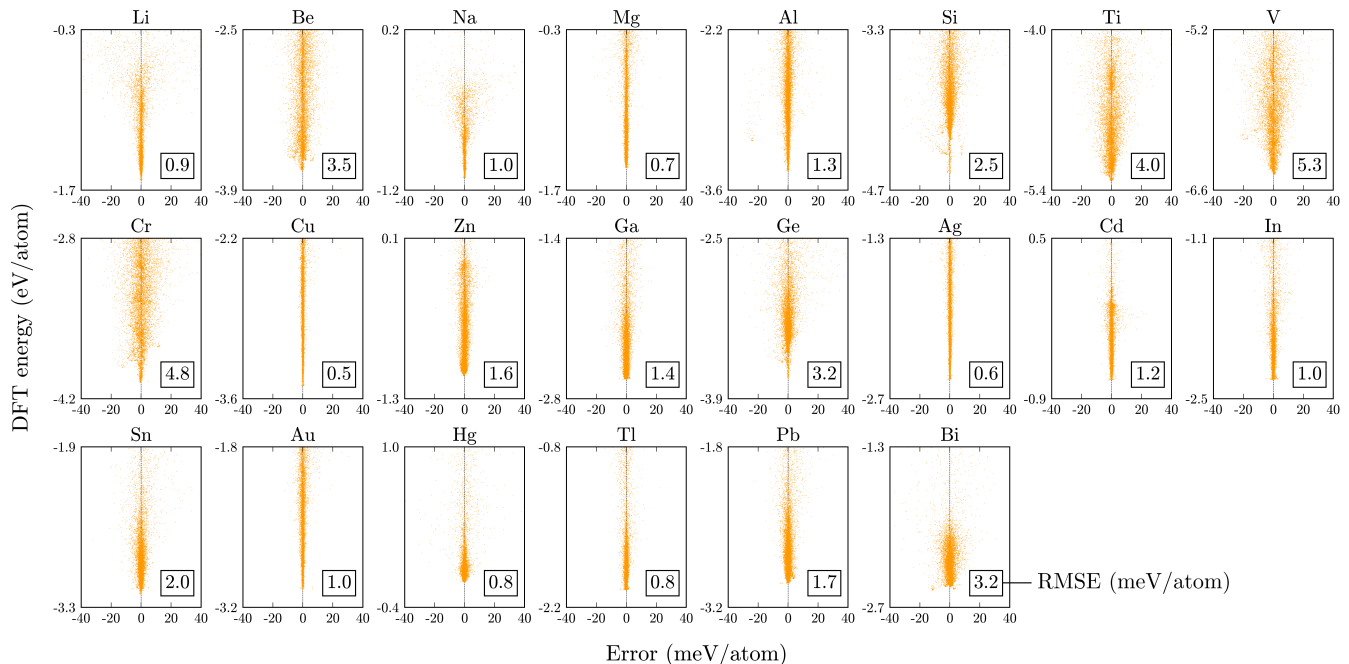


FIG. 1. Distribution of the energies of structures in the training and test datasets computed using the DFT calculation and those calculated using the polynomial MLP, which has the lowest prediction error. The vertical axis range is fixed to 1.4 eV/atom, although structures with energy values higher than the energy range are included in the datasets. The numerical values enclosed in the squares represent the root square mean errors (RMSEs) for the energy, which are estimated using the test datasets.

pendix A were utilized to perform AIMD simulations, and these PAW potentials include scalar-relativistic corrections. These PAW potentials were the same as those used for constructing the polynomial MLPs. The DFT calculations were performed without considering spin-orbit coupling.

### C. Structural quantities for liquid states

#### 1. Radial distribution function

The radial distribution function (RDF), denoted as  $g(r)$ , has been widely used for describing liquid structures quantitatively [57, 58]. The RDF characterizes the spatial distribution of atoms as a function of distance  $r$  from a reference atom relative to the probability for a completely random distribution. In practice, the RDF is approximately calculated as a histogram with a given bin width. Here, we use the bin width of 0.1 Å to evaluate the RDF.

#### 2. Bond-angle distribution function

The bond-angle distribution function (BADF), denoted as  $g(\theta)$ , has been employed to analyze the local orientational order in liquid and disordered states [59–61]. The BADF can be defined as the probability distri-

bution of bond angles formed by two neighboring atoms within a given cutoff distance. In this study, the cutoff distance is given as 1.4 times the distance corresponding to the first peak in the RDF. Moreover, the BADF is also practically evaluated as a histogram using the bin width of one degree.

#### 3. Running coordination number

The coordination number is often given as the integration of the RDF up to the distance corresponding to the first minimum in the RDF [8, 38, 60]. However, it is problematic to determine the distance of the first minimum precisely in some systems exhibiting flat first minima. In such a case, the coordination number cannot be estimated robustly because of the uncertainty of the first minimum position. Therefore, we employ the running coordination number (CN) [58] as a structural quantity, which is defined as

$$N_{\text{cn}}(r) = \frac{4\pi N}{V} \int_0^r \tilde{r}^2 g(\tilde{r}) d\tilde{r}, \quad (11)$$

where  $N$  is the number of atoms in the system, and  $V$  is the system volume. The running CN provides the average number of atoms coordinating a given atom out to a distance  $r$ .

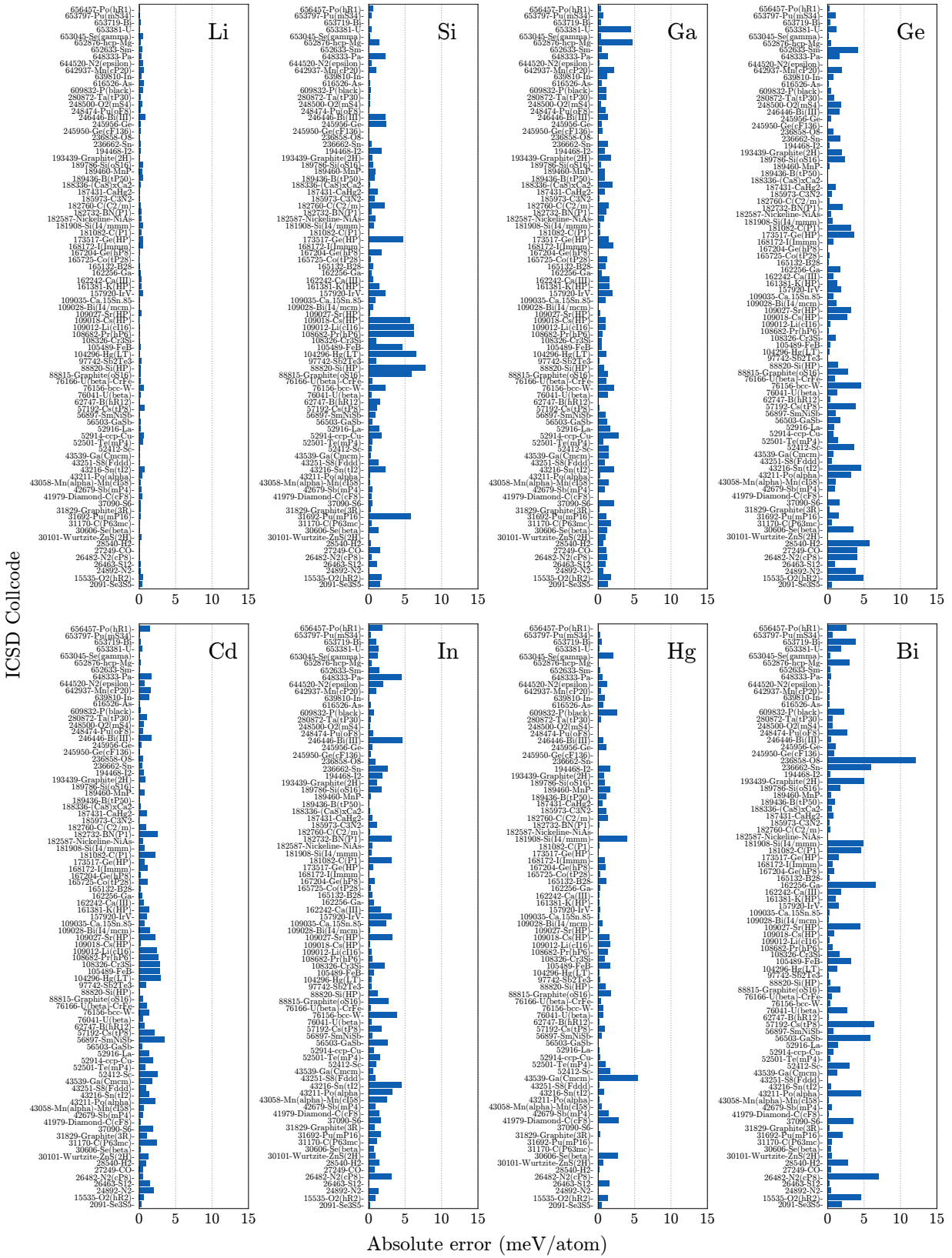


FIG. 2. Absolute prediction errors of the cohesive energy for 86 prototype structures in elemental Li, Si, Ga, Ge, Cd, In, Hg, and Bi. The absolute prediction errors for the other systems can be found in the supplemental material.

#### 4. Bond-orientational order parameters

The bond-orientational order parameters (BOOPs) proposed by Steinhardt *et al.* [62] have been used for characterizing the local orientational order in liquid and disordered states [63–65]. The BOOPs are equivalent to second-order polynomial invariants of spherical harmonics with any rotation. Therefore, the definition of the BOOPs is similar to the second-order polynomial invariants used in the polynomial MLPs. The order parameter around the central atom  $i$ ,  $Q_l(i)$ , is given by second-order polynomial invariants of  $Q_{lm}(i)$  as

$$Q_l(i) = \sqrt{\frac{4\pi}{2l+1} \sum_{m=-l}^l |Q_{lm}(i)|^2}, \quad (12)$$

where  $Q_{lm}(i)$  denotes the spherical harmonic functions  $Y_{lm}$  averaged over its neighboring atoms described by

$$Q_{lm}(i) = \frac{1}{N_{\text{neigh}}} \sum_{j \in \text{neighbor}} Y_{lm}(\theta_{ij}, \varphi_{ij}). \quad (13)$$

Angles  $\theta_{ij}$  and  $\varphi_{ij}$  give the azimuthal and polar angles of the spherical coordinates of neighboring atom  $j$  centered at the position of atom  $i$ . The BOOP of angular number  $l$  is then defined as the average of  $Q_l(i)$  over all atoms, expressed as

$$Q_l = \frac{1}{N} \sum_{i=1}^N Q_l(i). \quad (14)$$

We employ the ensemble average of the BOOP,  $\langle Q_l \rangle$ , as a structural quantity. The neighboring atoms are determined using the cutoff distance given as 1.4 times the distance corresponding to the first peak in the RDF.

### III. RESULTS AND DISCUSSION

#### A. Si and Ge

In elemental Si, we perform MD simulations at six temperatures below and above its melting temperature of 1687 K [66], i.e., 1600, 1750, 1900, 2050, 2200, and 2350 K, using the Pareto-optimal polynomial MLPs, other interatomic potentials in the literature, and the DFT calculation. In elemental Ge, we also perform MD simulations at six temperatures below and above its melting temperature of 1211 K [66], i.e., 1150, 1300, 1450, 1600, 1750, and 1900 K.

We define the RDF error in a quantitative manner as

$$(\text{RDF error}) = \frac{1}{n_{\text{bin}}} \sum_{t=1}^{n_{\text{bin}}} \left| \frac{g_{\text{pot}}(r_t) - g_{\text{DFT}}(r_t)}{(g_{\text{pot}}(r_t) + g_{\text{DFT}}(r_t))/2} \right|, \quad (15)$$

where  $g_{\text{pot}}(r_t)$  and  $g_{\text{DFT}}(r_t)$  are the frequencies of the single bin centered at  $r_t$  in the RDF histogram obtained using an interatomic potential and that obtained using the DFT calculation, respectively. The number of bins is denoted by  $n_{\text{bin}}$ . This error metric is known as the symmetric mean absolute percentage error [67]. In this metric, division by zero occurs when both  $g_{\text{pot}}(r_t)$  and  $g_{\text{DFT}}(r_t)$  are equal to zero. Hence, we exclude such bins to calculate the RDF error. Figure 3(a) shows the mean RDF errors of the polynomial MLPs, calculated by averaging the RDF errors at the six temperatures. As found in Fig. 3(a), the mean RDF error decreases as the model complexity of polynomial MLP increases, and there is a strong correlation between the mean RDF error and the prediction error for the test dataset.

Figure 3(b) shows the RDFs and BADFs computed using the three polynomial MLPs highlighted in Fig. 3(a) at 1750 and 1300 K in Si and Ge, respectively. They are compared with the RDFs and BADFs obtained using the DFT calculation. The RDFs computed using other polynomial MLPs are shown in the supplemental material. As seen in Fig. 3(b), the RDFs and BADFs obtained using MLP (1), showing the largest mean RDF error among the three MLPs, are slightly different from those obtained using the DFT calculation. On the other hand, the RDFs and BADFs calculated using the other MLPs almost overlap with those obtained using the DFT calculation.

Figure 4 shows the RDFs and BADFs calculated using the polynomial MLPs at the six temperatures in Si and Ge, as well as those obtained using the DFT calculation. The running CNs and BOOPs are also calculated at 1750 and 1300 K in Si and Ge, respectively. Here, the polynomial MLP showing the lowest mean RDF error is employed for each system. In Fig. 4, the structural quantities calculated using the empirical interatomic potentials of the Tersoff potentials [68, 69] and the modified EAM (MEAM) potentials [70, 71] are also shown for comparison. In addition, we calculate the structural quantities using the other MLPs of the quadratic SNAPs [72] that are available in the interatomic potential repository for Si and Ge [50, 51] and similar to the polynomial MLPs [34, 35].

In elemental Si, the structural quantities computed using the polynomial MLP are consistent with the DFT structural quantities at temperatures below and above the melting temperature. The structural quantities calculated using the quadratic SNAP [72] are also close to the DFT structural quantities. However, the predictive power of the quadratic SNAP decreases at temperatures close to the melting temperature. More quantitatively, the RDF errors computed using the polynomial MLP and the quadratic SNAP at the lowest temperature among the six temperatures are 0.021 and 0.105, respectively, while those at the highest temperature among the six temperatures are 0.018 and 0.058, respectively. In temperatures close to the melting temperature, more complex descriptions of the potential energy should be re-

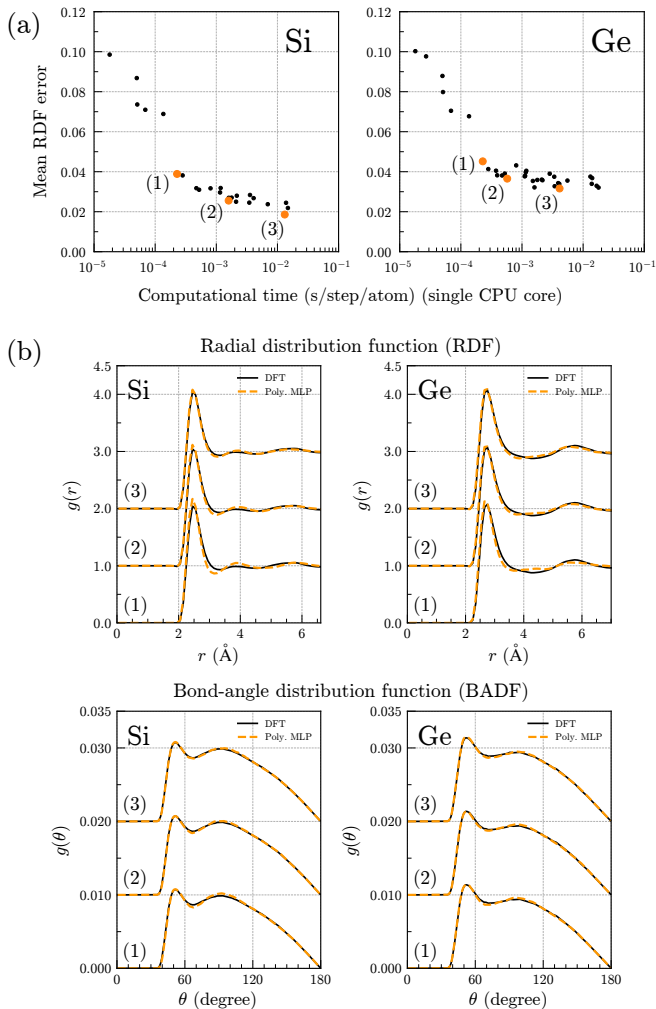


FIG. 3. (a) Mean RDF errors of the polynomial MLPs in Si and Ge. The mean RDF error was calculated by averaging the RDF errors at the six temperatures. The computational time on the horizontal axis is regarded as the model complexity of the polynomial MLP. (b) RDFs and BADFes computed using the three polynomial MLPs, (1), (2), and (3), highlighted in (a) at 1750 and 1300 K in Si and Ge, respectively. The RDFs and BADFes at each polynomial MLP are shifted upwards by the amounts of 1.0 and 0.01, respectively. The black solid and orange dotted lines indicate the distribution functions computed using the DFT calculation and the polynomial MLP, respectively.

quired than those at higher temperatures, where the detailed shape of the potential energy is less important. Regarding the empirical potentials, the structural quantities computed using the Tersoff [68] and MEAM [70] potentials are similar to but inconsistent with the DFT structural quantities. In particular, ghost second peaks are recognized in the RDFs, and the peak intensities of the BADFes differ from those of the DFT calculation. In addition, the running CNs deviate slightly from those of the DFT calculation, and the BOOPs are overestimated for small  $l$  values.

In elemental Ge, the structural quantities computed using the polynomial MLP agree with the DFT structural quantities at all six temperatures. The structural quantities calculated using the quadratic SNAP [72] are also close to the DFT structural quantities. However, the predictive power of the quadratic SNAP decreases at temperatures close to the melting temperature, as seen in the case of Si. The RDF errors computed using the polynomial MLP and the quadratic SNAP at the lowest temperature among the six temperatures are 0.051 and 0.125, whereas those at the highest temperature among the six temperatures are 0.033 and 0.059, respectively. Regarding the empirical potentials, the structural quantities computed using the Tersoff [69] and MEAM [71] potentials fail to reconstruct the peak positions and intensities of the RDFs and BADFes. The running CNs calculated using the Tersoff and MEAM potentials exhibit plateaus at around 3.0 Å and 3.5 Å, respectively, and these  $r$  values correspond to the first minimum positions in the RDFs. These plateaus are not found in the running CN of the DFT calculation. The BOOPs calculated using the MEAM potential exhibit two peaks, which differ from the BOOPs obtained using the DFT calculation. The current polynomial MLPs are confirmed to exhibit high predictive power for the liquid structural properties in these systems. On the other hand, the empirical potentials fail to predict the liquid structural properties accurately.

Note that we regard liquid structural quantities obtained from our DFT calculations as the correct ones throughout this study and then compare structural quantities calculated using various interatomic potentials. However, it is challenging to fairly compare the predictive powers of the current polynomial MLPs and interatomic potentials developed elsewhere because different training datasets are regarded as the correct datasets. When an interatomic potential is developed from a DFT training dataset, the interatomic potential depends on the computational method and conditions of the DFT calculation, including the selection of the exchange-correlation functional and PAW potential. Also, some interatomic potentials were developed using experimental training data. Such interatomic potentials can include deviations from our DFT calculations. We have employed typical computational settings for the DFT calculation; hence, it may be fair to say that the present polynomial MLPs can predict liquid structural properties with the same accuracy as those of typical DFT calculations.

## B. Li, Be, Na, and Mg

Figures 5, 6, 7, and 8 show the structural quantities calculated from MD simulations using the polynomial MLPs for Li, Be, Na, and Mg, respectively. The RDFs and BADFes are computed at three temperatures above the melting temperatures of 454, 1560, 371, and 923 K [66] in elemental Li, Be, Na, and Mg, respectively.

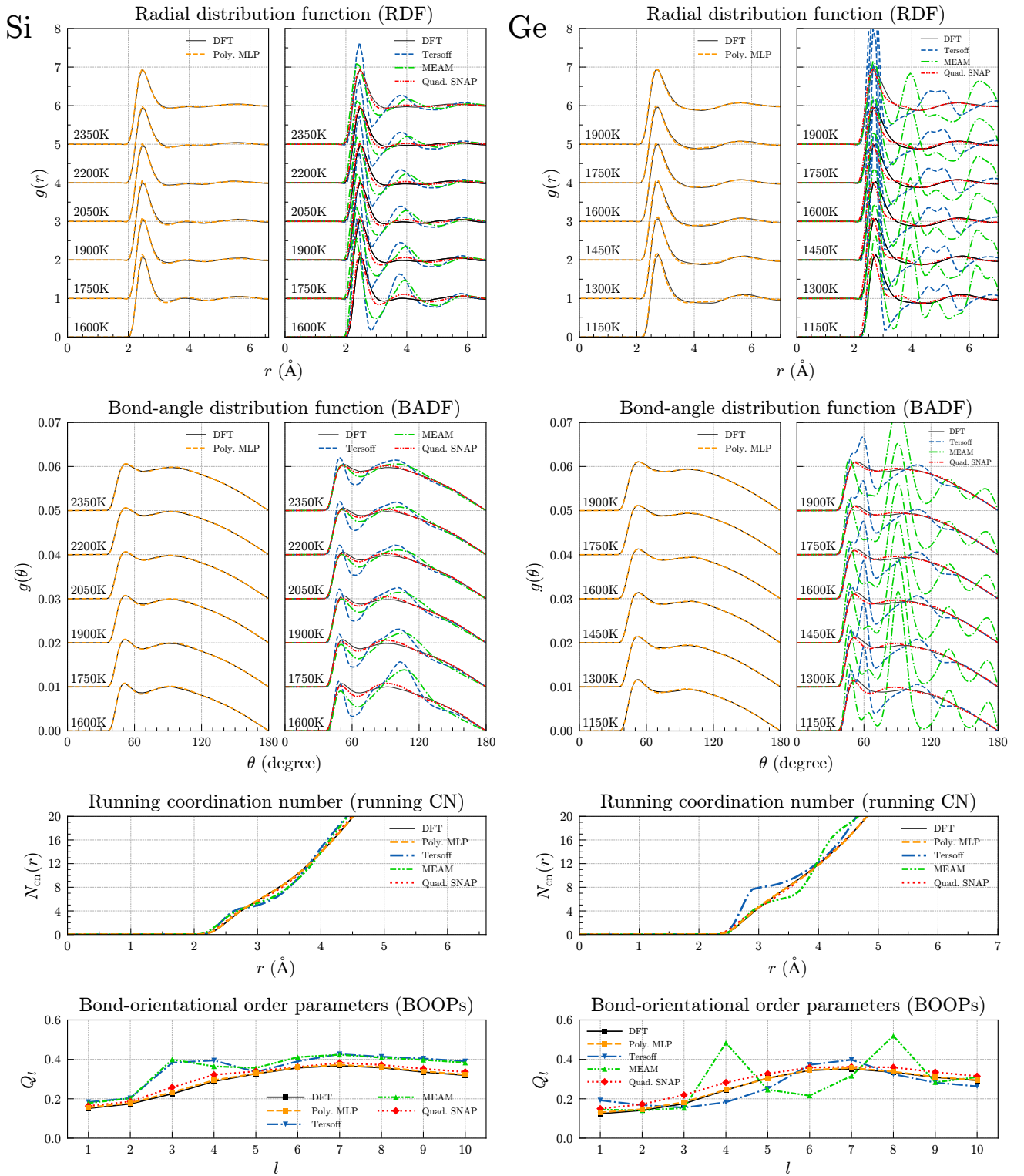


FIG. 4. RDFs, BADFs, running CNs, and BOOPs obtained from MD simulations using the polynomial MLPs in elemental Si and Ge. The polynomial MLP showing the lowest mean RDF error is employed for each system. The structural quantities calculated using the DFT calculation, the Tersoff potentials [68, 69], the MEAM potentials [70, 71], and the quadratic SNAPs [72] are also shown for comparison. The RDFs and BADFs at each temperature are shifted upwards by the amounts of 1.0 and 0.01, respectively. The running CNs and BOOPs were calculated at 1750 and 1300 K in Si and Ge, respectively, which are close to their melting temperatures. The black solid and orange dotted lines indicate the structural quantities computed using the DFT calculation and the polynomial MLP, respectively. In the legend, Poly. MLP and Quad. SNAP stand for polynomial MLP and quadratic SNAP, respectively.

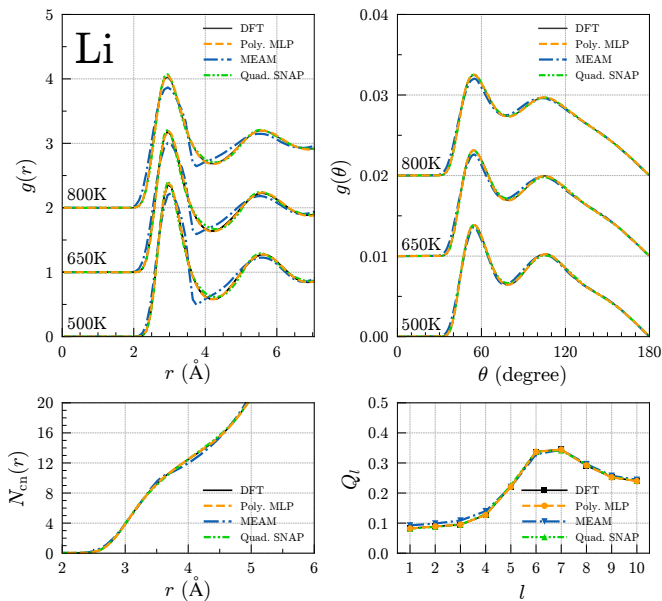


FIG. 5. Structural quantities obtained from MD simulations using the polynomial MLP in elemental Li. The polynomial MLP showing the lowest mean RDF error was employed. The structural quantities calculated using the DFT calculation, the MEAM potential [73], and the quadratic SNAP [72] are also shown for comparison. The RDFs and BADFs shown in the top-left and top-right panels, respectively, were obtained at three temperatures above the melting temperature. The RDFs and BADFs at each temperature are shifted upwards by the amounts of 1.0 and 0.01, respectively. The running CNs and BOOPs shown in the bottom-left and bottom-right panels, respectively, were calculated at the lowest temperature among the three temperatures, which was closest to the melting temperature. The black solid and orange dotted lines indicate the structural quantities computed using the DFT calculation and the polynomial MLP, respectively. In the legend, Poly. MLP and Quad. SNAP stand for polynomial MLP and quadratic SNAP, respectively.

The running CNs and BOOPs at the lowest temperature among the three temperatures, which is the closest to the melting temperature, are also shown. The structural quantities of the polynomial MLPs are consistent with the DFT structural quantities in Li, Be, Na, and Mg.

In elemental Li, the RDFs of the MEAM potential [73] slightly deviate from those of the DFT calculation. However, the other structural quantities of the MEAM potential and all structural quantities of the quadratic SNAP [72] are compatible with the DFT structural quantities. In elemental Na, the structural quantities of the EAM [76] and MEAM [77] potentials are close to the DFT structural quantities. In elemental Mg, the EAM potentials [78, 79] and DFT calculation yield consistent structural quantities.

Although the empirical potentials in Li, Na, and Mg accurately predict the liquid structural quantities, the structural quantities computed using the empirical potentials of the EAM [74] and MEAM [75] potentials are

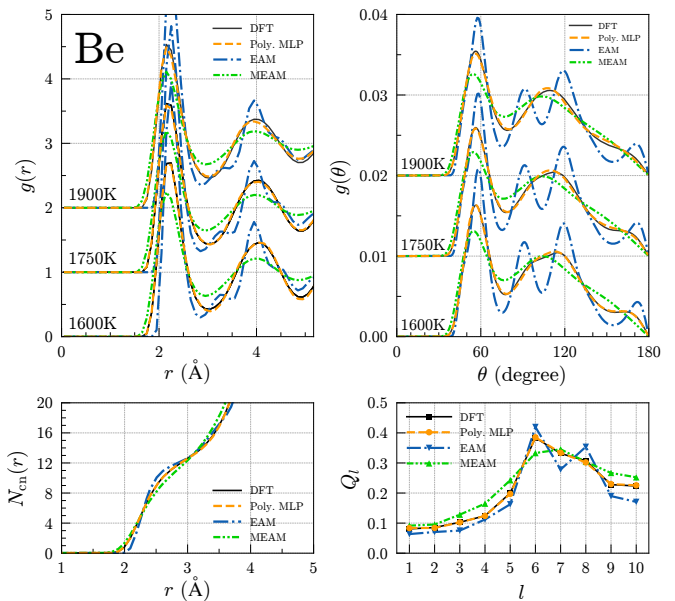


FIG. 6. Structural quantities calculated using the DFT calculation, the polynomial MLP, the EAM potential [74], and the MEAM potential [75] in elemental Be.

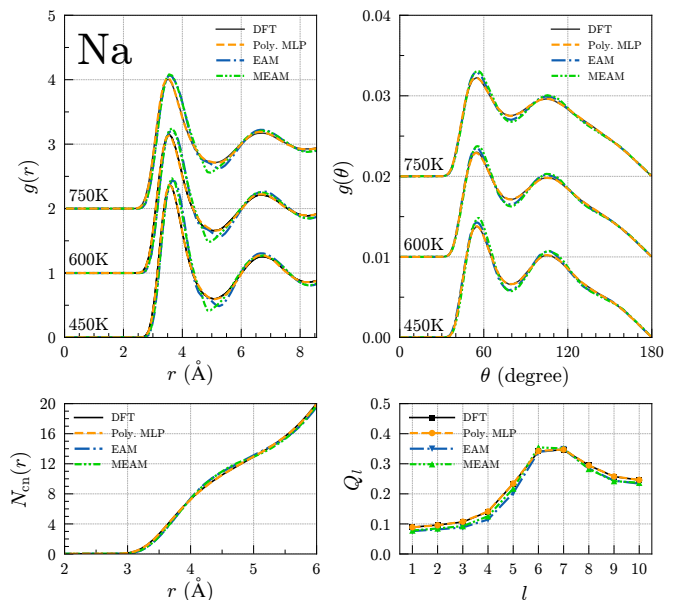


FIG. 7. Structural quantities calculated using the DFT calculation, the polynomial MLP, the EAM potential [76], and the MEAM potential [77] in elemental Na.

inconsistent with the DFT structural quantities in Be. Although the EAM and MEAM potentials qualitatively predict correlations in the RDFs, the peak intensities in the RDFs differ from those of the DFT calculation. Also, three peaks recognized between 45 and 135 degrees in the BADFs of the EAM potential are not found in those of the DFT calculation. The shape of the BADFs calculated using the MEAM potential does not exhibit such ghost

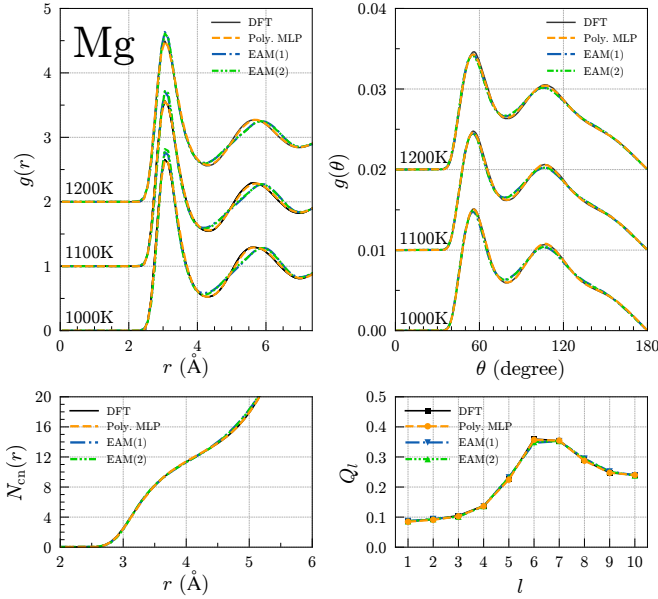


FIG. 8. Structural quantities calculated using the DFT calculation, the polynomial MLP, and the EAM potentials [78, 79] in elemental Mg.

peaks, but the peak intensities of the MEAM potential and the DFT calculation are different. In addition, the running CNs and BOOPs computed using the EAM and MEAM potentials differ from those computed using the DFT calculation.

The RDFs computed using all other Pareto-optimal polynomial MLPs at the lowest temperature among the three temperatures are shown in the supplemental material. Most of the polynomial MLPs yield accurate RDFs, except for simplistic polynomial MLPs. Although here we demonstrate only the liquid quantities calculated using the polynomial MLP with the lowest mean RDF error, the above discussion on the predictive power for liquid structures is independent of the selection of the polynomial MLP.

### C. Ti, V, and Cr

Figures 9, 10, and 11 show the structural quantities calculated from MD simulations at three temperatures using the polynomial MLPs and other empirical potentials for Ti, V, and Cr, respectively. The RDFs and BADFs are computed at three temperatures above the melting temperatures of 1941, 2183, and 2180 K [66] in elemental Ti, V, and Cr, respectively. The running CNs and BOOPs at the lowest temperature among the three temperatures, which is the closest to the melting temperature, are also shown. The structural quantities of the polynomial MLPs agree with the DFT structural quantities. The RDFs calculated using other polynomial MLPs are shown in the supplemental material and indicate that most of the polynomial MLPs have high predictive power

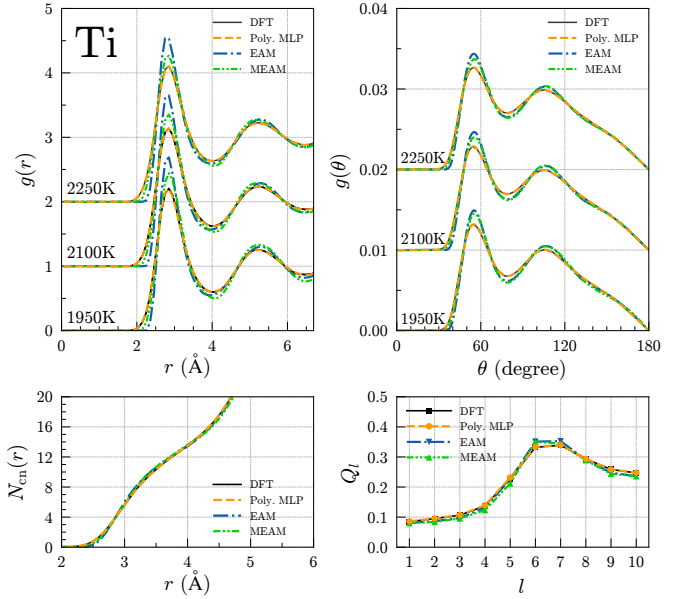


FIG. 9. Structural quantities calculated using the DFT calculation, the polynomial MLP, EAM potential [80], and MEAM potential [81] in elemental Ti.

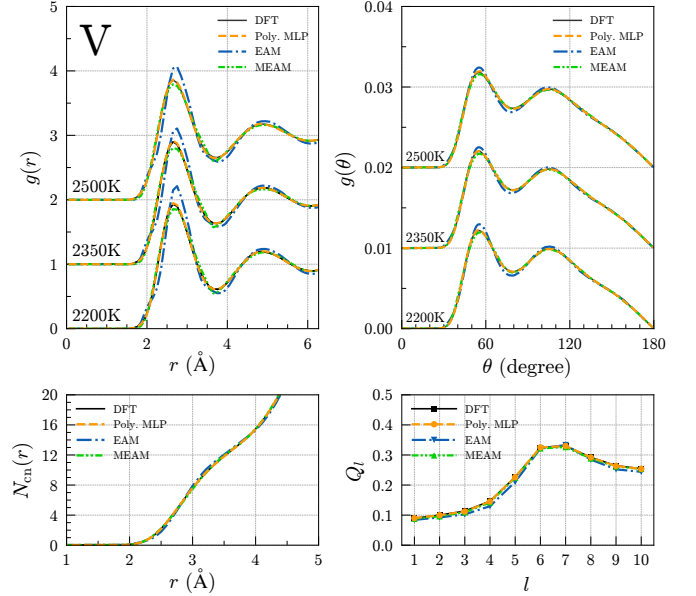


FIG. 10. Structural quantities calculated using the DFT calculation, the polynomial MLP, EAM potential [82], and MEAM potential [83] in elemental V.

for liquid structural properties.

The EAM [80] and MEAM [81] potentials exhibit similar structural quantities in elemental Ti. However, the peak intensities of the RDFs and BADFs differ slightly from the DFT ones. In elemental V, the RDFs of the EAM [82] potential slightly deviate from those of the DFT calculation, while the MEAM [83] potential achieves accurate predictions for all structural quanti-

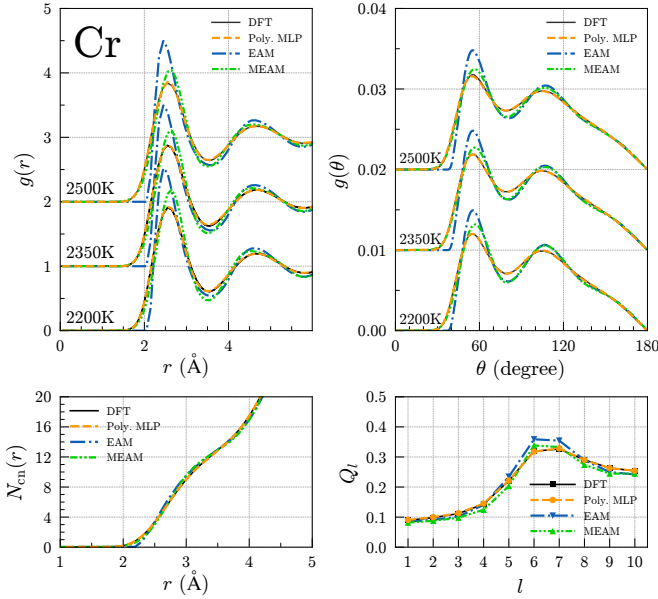


FIG. 11. Structural quantities calculated using the DFT calculation, the polynomial MLP, EAM potential [84], and MEAM potential [83] in elemental Cr.

ties. The running CN and BOOPs of the MEAM potential [83] are close to the DFT structural quantities in elemental Cr. However, the peak intensities of the RDFs and BADFs differ slightly from those computed from the DFT calculation. The EAM potential [84] shows less accurate structural quantities than the MEAM potential.

#### D. Cu, Ag, and Au

Figures 12, 13, and 14 show the structural quantities calculated from MD simulations at three temperatures using the polynomial MLPs and other interatomic potentials for Cu, Ag, and Au, respectively. The RDFs and BADFs are computed at three temperatures above the melting temperatures of 1358, 1235, and 1337 K [66] in elemental Cu, Ag, and Au, respectively. The running CNs and BOOPs at the lowest temperature among the three temperatures, which is the closest to the melting temperature, are also shown. The structural quantities of the polynomial MLPs are comparable to the DFT structural quantities in Cu, Ag, and Au. The RDFs calculated using other polynomial MLPs are shown in the supplemental material and indicate that most of the polynomial MLPs have high predictive power for liquid structural properties.

In elemental Cu, the structural quantities of the MEAM potential [85] agree with the DFT ones. The quadratic SNAP [72] also reconstructs the DFT structural quantities accurately. In elemental Ag and Au, all the empirical potentials [80, 86–88] yield accurate structural quantities.

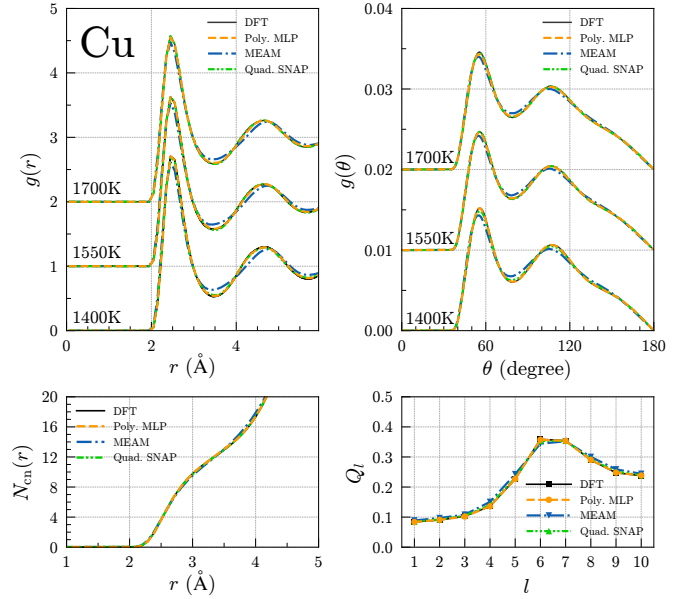


FIG. 12. Structural quantities calculated using the DFT calculation, the polynomial MLP, the MEAM potential [85], and quadratic SNAP [72] in elemental Cu.

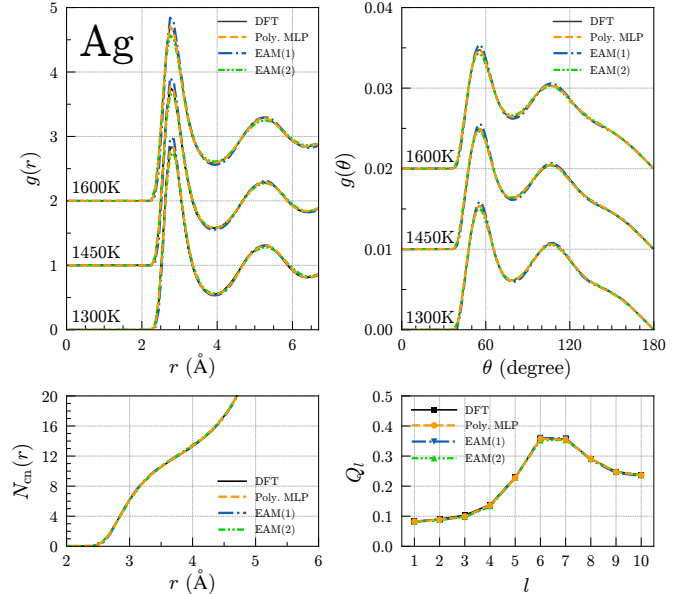


FIG. 13. Structural quantities calculated using the DFT calculation, the polynomial MLP, and the EAM potentials [80, 86] in elemental Ag.

#### E. Zn, Cd, and Hg

Figures 15, 16, and 17 show the structural quantities calculated from MD simulations at three temperatures using the polynomial MLPs and other empirical potentials for Zn, Cd, and Hg, respectively. The RDFs and BADFs are computed at three temperatures above the melting temperatures of 693, 594, and 234 K [66] in el-

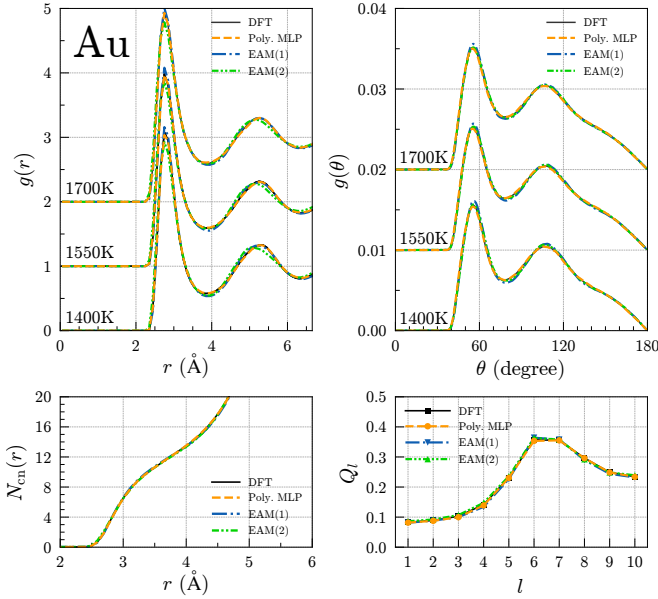


FIG. 14. Structural quantities calculated using the DFT calculation, the polynomial MLP, and the EAM potentials [87, 88] in elemental Au.

elemental Zn, Cd, and Hg, respectively. The running CN and BOOPs at the lowest temperature among the three temperatures, which is the closest to the melting temperature, are also shown. The structural quantities of the polynomial MLPs are consistent with the DFT structural quantities. The RDFs calculated using other polynomial MLPs are shown in the supplemental material and indicate that most of the polynomial MLPs have high predictive power for liquid structural properties.

In elemental Zn, the LJ potential [89] is a simple model with potential energy depending solely on the distance between two atoms; hence, it fails to reconstruct the peak positions of the RDFs, the peak intensities of the BADFs, and the running CN of the DFT calculation. The MEAM potential [90] shows structural quantities better than the LJ potential but fails to reconstruct the peak positions of the RDFs and the peak intensities of the BADFs, similarly to the LJ potential. In elemental Cd, the BO potential [92] fails to accurately predict the peak positions of the RDFs and the peak intensities of the BADFs. On the other hand, structural quantities computed using the EAM potential [91] agree well with the DFT structural quantities. In elemental Hg, the accuracy of the LJ potential [89] for the structural quantities is worse than in Zn, and in particular, the LJ potential fails to reconstruct the BOOPs. The SW potential [93] also fails to predict the DFT structural quantities.

### F. Al, Ga, In, and Tl

Figures 18, 19, 20, and 21 show the structural quantities calculated from MD simulations at three temper-

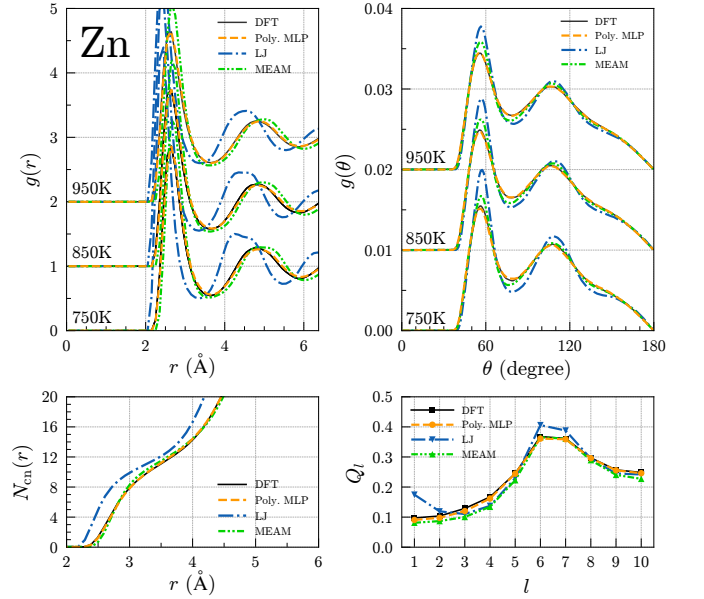


FIG. 15. Structural quantities calculated using the DFT calculation, the polynomial MLP, the LJ potential [89], and MEAM potential [90] in elemental Zn.

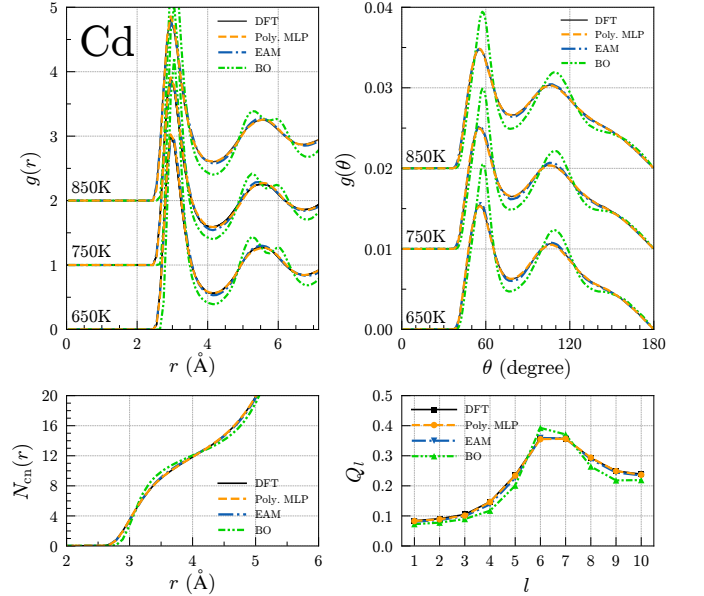


FIG. 16. Structural quantities calculated using the DFT calculation, the polynomial MLP, the EAM potential [91], and BO potential [92] in elemental Cd.

atures using the polynomial MLPs and other empirical potentials for Al, Ga, In, and Tl, respectively. The RDFs and BADFs are computed at three temperatures above the melting temperatures of 933, 303, 430, and 577 K [66] in elemental Al, Ga, In, and Tl, respectively. The running CNs and BOOPs at the lowest temperature among the three temperatures, which is the closest to the melting temperature, are also shown. The structural quanti-

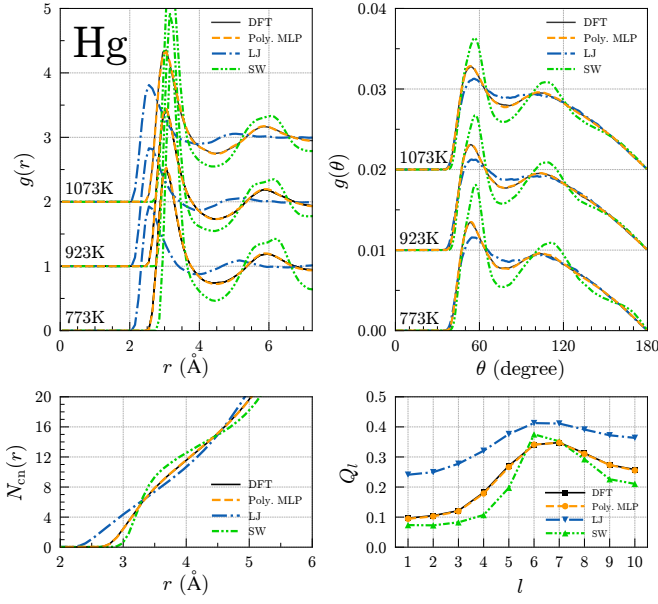


FIG. 17. Structural quantities calculated using the DFT calculation, the polynomial MLP, the LJ potential [89], and SW potential [93] in elemental Hg.

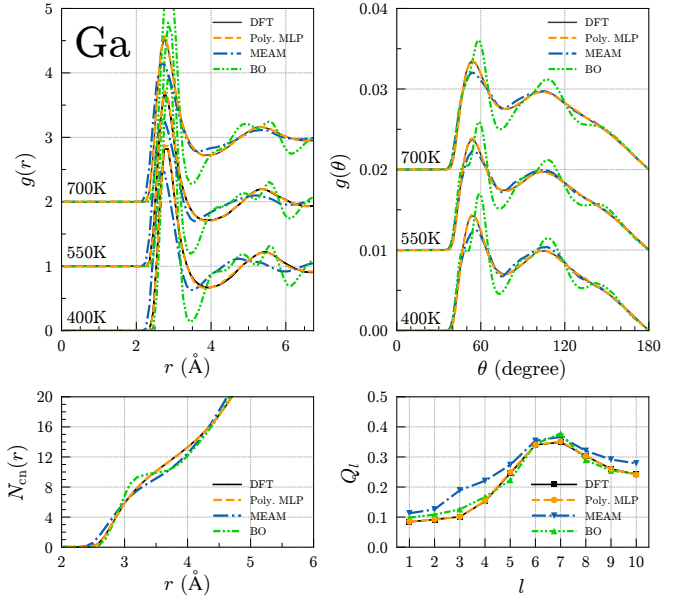


FIG. 19. Structural quantities calculated using the DFT calculation, the polynomial MLP, the MEAM potential [95], and BO potential [96] in elemental Ga.

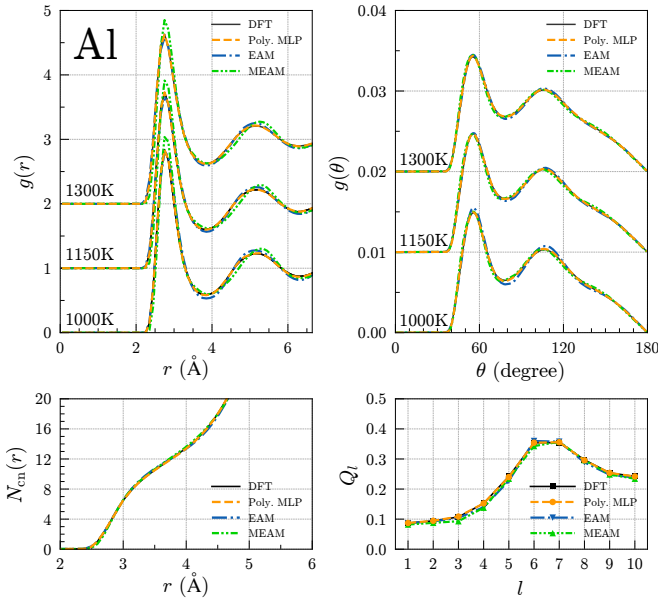


FIG. 18. Structural quantities calculated using the DFT calculation, the polynomial MLP, the EAM potential [87], and MEAM potential [94] in elemental Al.

ties of the polynomial MLPs agree with the DFT structural quantities. The RDFs calculated using other polynomial MLPs are shown in the supplemental material and indicate that most of the polynomial MLPs have high predictive power for liquid structural properties.

In elemental Al, although the RDFs of the MEAM potential [94] slightly differ from those of the DFT calculation, the other structural quantities of the MEAM po-

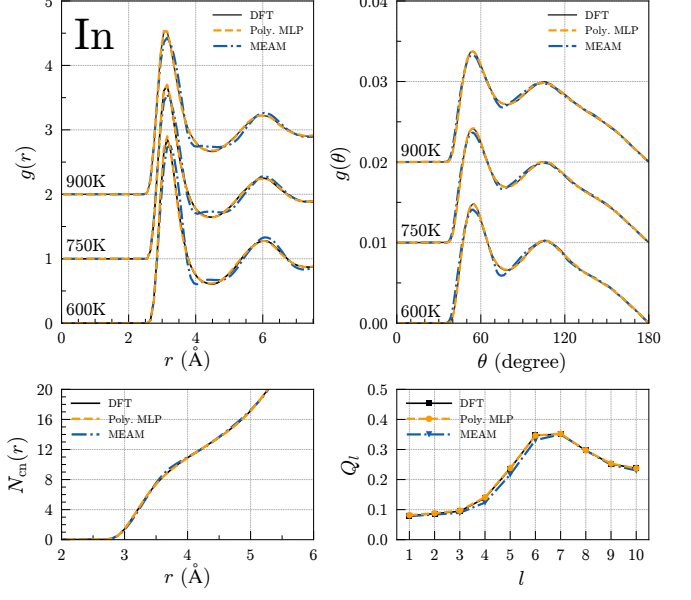


FIG. 20. Structural quantities calculated using the DFT calculation, the polynomial MLP, and MEAM potential [97] in elemental In.

tential and all structural quantities of the EAM potential [87] are consistent with the DFT structural quantities. In elemental Ga, the MEAM potential [95] cannot accurately reproduce all structure quantities calculated using the DFT calculation. The RDFs, BADFs, and running CNs computed using the BO potential [96] are less accurate than those computed using the MEAM potential. In elemental In, the MEAM potential [97] results are close to the DFT structural quantities. In elemental Tl, the

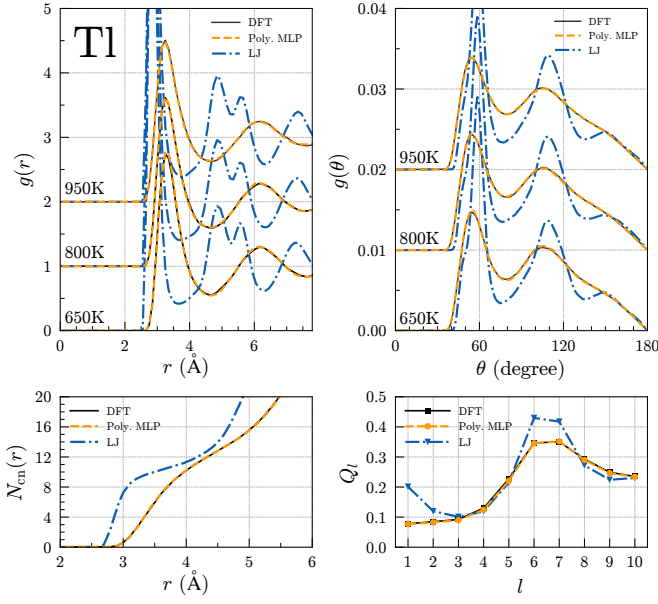


FIG. 21. Structural quantities calculated using the DFT calculation, the polynomial MLP, and the LJ potential [89] in elemental Tl.

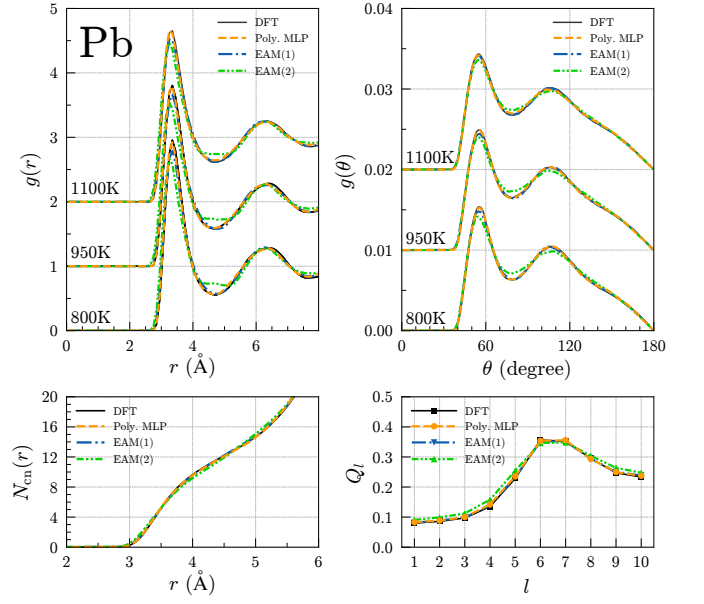


FIG. 23. Structural quantities calculated using the DFT calculation, the polynomial MLP, and EAM potentials [80, 99] in elemental Pb.

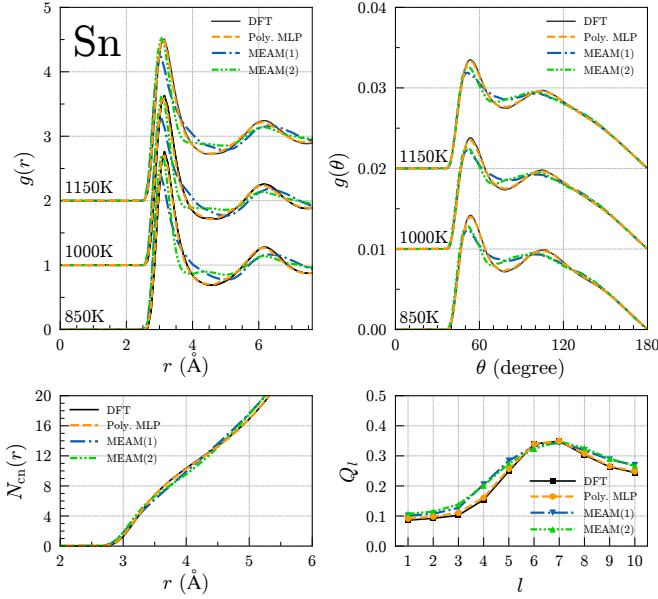


FIG. 22. Structural quantities calculated using the DFT calculation, the polynomial MLP, and MEAM potentials [77, 98] in elemental Sn.

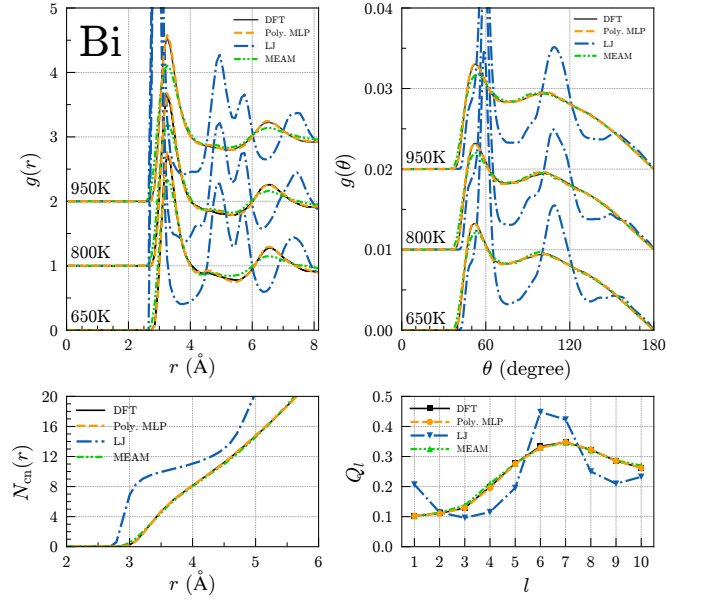


FIG. 24. Structural quantities calculated using the DFT calculation, the polynomial MLP, LJ potential [89], and MEAM potential [100] in elemental Bi.

LJ potential [89] shows incorrect structural quantities.

### G. Sn, Pb, and Bi

Figures 22, 23, and 24 show the structural quantities calculated from MD simulations at three temperatures using the polynomial MLPs and other empirical potentials for Sn, Pb, and Bi, respectively. The RDFs and

BADFs are computed at three temperatures above the melting temperatures of 505, 601, and 544 K [66] in elemental Sn, Pb, and Bi, respectively. The running CNs and BOOPs at the lowest temperature among the three temperatures, which is the closest to the melting temperature, are also shown. The structural quantities of the polynomial MLPs are consistent with the DFT structural quantities. The RDFs calculated using other polynomial MLPs are shown in the supplemental material and indi-

TABLE I. RDF errors computed using interatomic potentials at the lowest temperature among our temperature settings. Poly. MLP and Quad. SNAP stand for polynomial MLP and quadratic SNAP, respectively.

Element	Potential	RDF error	Element	Potential	RDF error	Element	Potential	RDF error
Li	Poly. MLP	0.007	Cr	Poly. MLP	0.011	Sn	Poly. MLP	0.035
	Quad. SNAP [72]	0.036		MEAM [83]	0.141		MEAM(1) [98]	0.175
	MEAM [73]	0.183		EAM [84]	0.380		MEAM(2) [77]	0.189
Be	Poly. MLP	0.030	Cu	Poly. MLP	0.014	Au	Poly. MLP	0.014
	MEAM [75]	0.339		Quad. SNAP [72]	0.033		EAM(1) [87]	0.041
	EAM [74]	0.418		MEAM [85]	0.097		EAM(2) [88]	0.064
Na	Poly. MLP	0.022	Zn	Poly. MLP	0.041	Hg	Poly. MLP	0.018
	MEAM [77]	0.135		MEAM [90]	0.210		SW [93]	0.402
	EAM [76]	0.147		LJ [89]	0.431		LJ [89]	0.438
Mg	Poly. MLP	0.017	Ga	Poly. MLP	0.019	Tl	Poly. MLP	0.019
	EAM(2) [79]	0.128		MEAM [95]	0.288		LJ [89]	0.685
	EAM(1) [78]	0.130		BO [96]	0.361			
Al	Poly. MLP	0.008	Ge	Poly. MLP	0.051	Pb	Poly. MLP	0.028
	EAM [87]	0.058		Quad. SNAP [72]	0.125		EAM(1) [80]	0.089
	MEAM [94]	0.118		Tersoff [69]	0.377		EAM(2) [99]	0.176
				MEAM [71]	0.491			
Si	Poly. MLP	0.021	Ag	Poly. MLP	0.016	Bi	Poly. MLP	0.023
	Quad. SNAP [72]	0.105		EAM(1) [86]	0.040		MEAM [100]	0.158
	Tersoff [68]	0.305		EAM(2) [80]	0.063		LJ [89]	0.650
	MEAM [70]	0.342						
Ti	Poly. MLP	0.012	Cd	Poly. MLP	0.015			
	MEAM [81]	0.221		EAM [91]	0.037			
	EAM [80]	0.288		BO [92]	0.320			
V	Poly. MLP	0.014	In	Poly. MLP	0.013			
	MEAM [83]	0.096		MEAM [97]	0.073			
	EAM [82]	0.156						

cate that most of the polynomial MLPs have high predictive power for liquid structural properties.

Two MEAM potentials [77, 98] exhibit running CNs and BOOPs similar to those of the DFT calculation in elemental Sn. However, the RDFs and BADFs of the MEAM potentials differ slightly from those of the DFT calculation. In elemental Pb, one EAM potential [80] can predict structural quantities accurately, while another EAM potential [99] shows less accurate structural quantities. In elemental Bi, the LJ potential [89] fails to reconstruct all structural quantities of the DFT calculation. On the other hand, the running CN and BOOPs computed using the MEAM potential [100] almost overlap with those obtained using the DFT calculation. However, the MEAM potential cannot accurately reproduce the RDFs and BADFs calculated using the DFT calculation.

### H. RDF errors

Table I summarizes the RDF errors computed using interatomic potentials at the lowest temperature among

our temperature settings. In all the systems, the RDF error for the polynomial MLP is the smallest, ranging approximately from 0.01 to 0.05. In elemental Li, Al, Cu, Ag, Cd, and Au, the values of the RDF errors are less than 0.06 for some interatomic potentials other than the polynomial MLP. These values of the RDF error are comparable to the mean RDF error shown in Fig. 3(a). As can be seen in Figs. 3(a) and (b), the interatomic potentials that exhibit RDF errors less than 0.06 reproduce the RDFs obtained from our DFT calculations accurately. In elemental Na, Mg, Si, V, Ge, In, and Pb, some interatomic potentials other than the polynomial MLP exhibit RDF errors ranging from 0.06 to 0.14. The accuracy of these potentials corresponds to that of simplistic polynomial MLPs with low computational costs. The empirical potentials show RDF errors larger than 0.14 in elemental Li, Be, Si, Ti, Cr, Zn, Ga, Ge, Sn, Hg, Tl, and Bi. These potentials fail to predict the RDFs accurately.

As pointed out in Sec. III A, interatomic potentials other than the polynomial MLPs sometimes include systematic deviations from our DFT calculations because of the use of different training datasets. However, some

TABLE II. Electronic configurations of selected PAW potentials that are considered as valence electrons.

Element	Valence states	Element	Valence states
Li	$2s^1$	Ga	$4s^24p^1$
Be	$2s^2$	Ge	$4s^24p^2$
Na	$3s^1$	Ag	$4d^{10}5s^1$
Mg	$3s^2$	Cd	$4d^{10}5s^2$
Al	$3s^23p^1$	In	$5s^25p^1$
Si	$3s^23p^2$	Sn	$5s^25p^2$
Ti	$3d^24s^2$	Au	$5d^{10}6s^1$
V	$3d^34s^2$	Hg	$5d^{10}6s^2$
Cr	$3d^54s^1$	Tl	$6s^26p^1$
Cu	$3d^{10}4s^1$	Pb	$6s^26p^2$
Zn	$3d^{10}4s^2$	Bi	$6s^26p^3$

empirical potentials yield RDFs that are totally different from RDFs obtained using our DFT calculations with typical computational settings. On the other hand, the polynomial MLPs exhibit minor RDF errors in all the elemental systems, which indicates that the polynomial MLPs can predict liquid structural properties with the same accuracy as those of reasonable DFT calculations.

#### IV. CONCLUSION

We examined the predictive power of the polynomial MLPs for structural properties in liquid states of 22 elemental systems. Structural quantities such as the RDF and BADF were used to compare the predictive power of the polynomial MLP and other interatomic potentials. The current polynomial MLPs were systematically developed from diverse crystal structures and their derivatives. No structural data in liquid states, such as structural trajectories in MD simulations at high temperatures, were used as training datasets. Nevertheless, they consistently exhibited high predictive power for the liquid structural properties in all 22 elemental systems of diverse chemical bonding properties. On the other hand, empirical potentials failed to predict liquid structural properties in many elemental systems where complex descriptions of the potential energy are required, such as Si, Ge, and Bi. Thus, we can conclude that the polynomial MLPs enable us to efficiently and accurately predict structural and dynamical properties not only in crystalline states but also in liquid and liquid-like disordered states.

#### ACKNOWLEDGMENTS

This work was supported by a Grant-in-Aid for Scientific Research (A) (Grant Number 21H04621), a Grant-in-Aid for Scientific Research (B) (Grant Number 22H01756), and a Grant-in-Aid for Scientific Research

on Innovative Areas (Grant Number 19H05787) from the Japan Society for the Promotion of Science (JSPS).

#### Appendix A: Selected PAW potentials

Table II summarizes the electronic configurations of selected PAW potentials that are considered as valence electrons. These PAW potentials were used to construct DFT datasets and perform AIMD simulations in this study.

#### Appendix B: Comparison with experimental profiles

##### 1. Si, Ga, Ge, and Bi

Here, we compare the structure factors and RDFs computed using interatomic potentials such as the polynomial MLP with experimentally reported ones. Figure 25 shows the structure factors and RDFs investigated in X-ray and neutron diffraction experiments in elemental Si, Ga, Ge, and Bi [101–106]. Experimental structure factors at similar temperatures are comparable in each system. However, the structure factor profiles show non-negligible differences. Similarly, experimental RDFs at almost the same temperatures are close to each other, but the first-peak intensities and the positions of the second peaks are inconsistent. Although experimental structure factors and RDFs are not uniquely given, we compare the structure factors and RDFs computed using the interatomic potentials with the experimental ones. In the supplemental material, the RDFs obtained using the polynomial MLPs are compared with those obtained using DFT calculations, reported in the literature [56, 109–121].

Figure 25 shows the structural factors and the RDFs obtained from MD simulations at 1703, 326, 1233, and 553 K, which are close to the melting temperatures, in elemental Si, Ga, Ge, and Bi, respectively. They were computed using the polynomial MLPs, quadratic SNAPs, and empirical interatomic potentials. In the MD simulations, we employed the simulation cell with 2744 atoms and the computational procedures described in Sec. II B. When using the quadratic SNAP [72] for the elemental Ge, we exceptionally employed the simulation cell with 216 atoms because several hundred attempts of MD simulations with larger simulation cells failed. The structure factor was obtained by Fourier transforming the corresponding RDF using

$$S(q) = 1 + \frac{4\pi N}{V} \int_0^{L_{\text{box}}/2} r^2(g(r) - 1) \frac{\sin(qr)}{qr} dr, \quad (\text{B1})$$

where  $L_{\text{box}}$  represents the simulation box length. This integral was evaluated using a histogram of the RDF with a bin width of 0.1 Å.

The structure factors of the polynomial MLP and quadratic SNAP [72] in elemental Si are similar to the experimental structure factors. However, they do not reconstruct the experimental structure factors around the

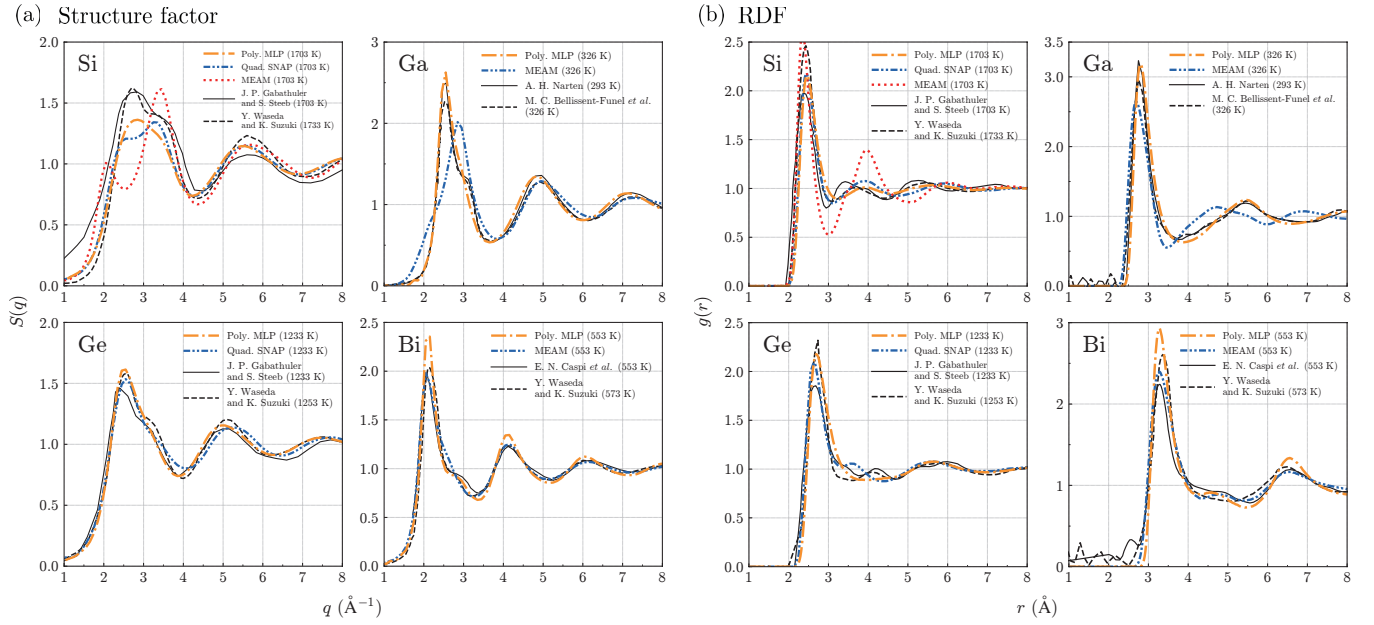


FIG. 25. (a) Structure factors computed using interatomic potentials such as the polynomial MLPs in elemental Si, Ga, Ge, and Bi, along with experimental structure factors revealed by X-ray and neutron diffraction investigations [101–106]. (Si [101, 102], Ga [103, 104], Ge [101, 102], Bi [105, 106]). (b) RDFs obtained using interatomic potentials in elemental Si, Ga, Ge, and Bi, along with experimental RDFs revealed by X-ray and neutron diffraction investigations [101–106].

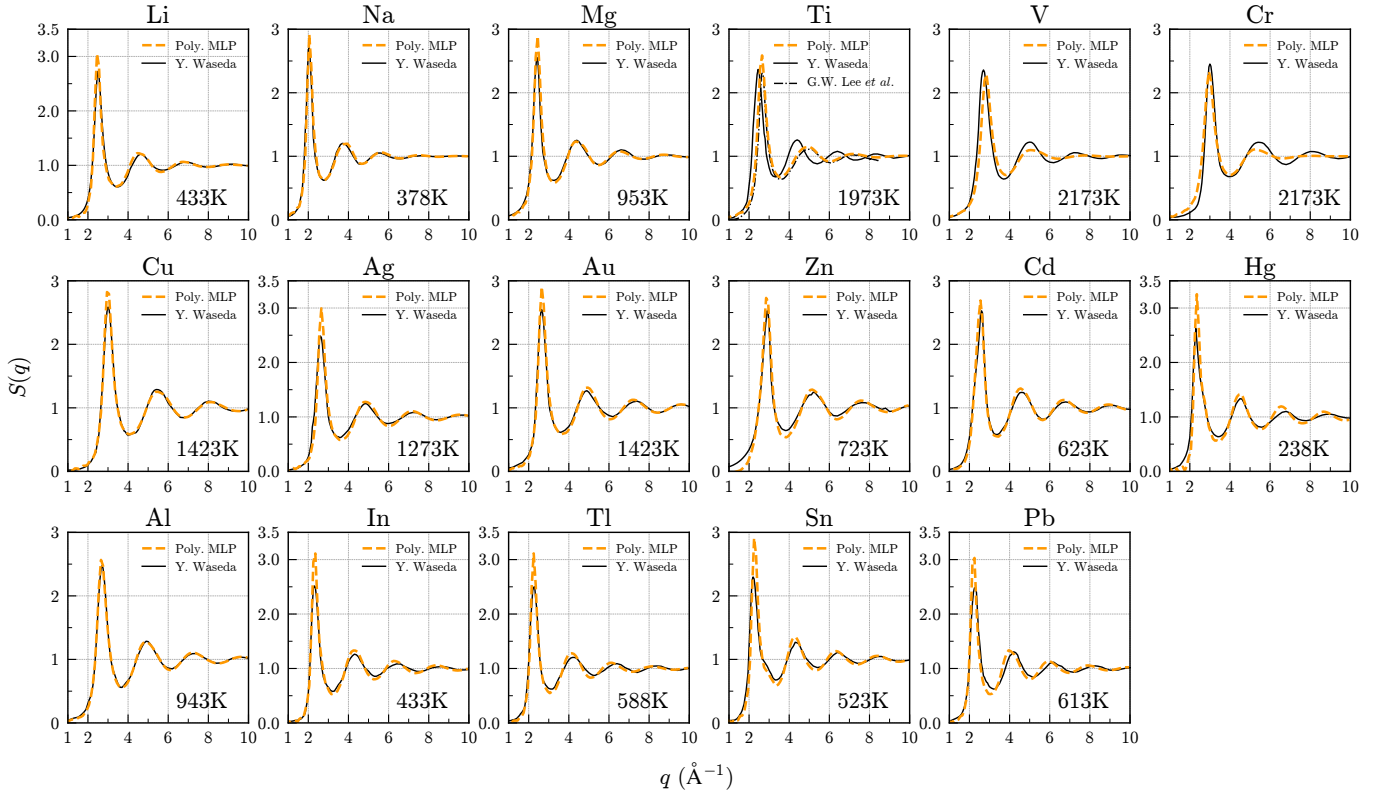


FIG. 26. Structure factors computed using the polynomial MLPs along with experimental structure factors revealed by X-ray diffraction investigations [107, 108].

first peak. On the other hand, the structure factors obtained using the polynomial MLP in elemental Ga and

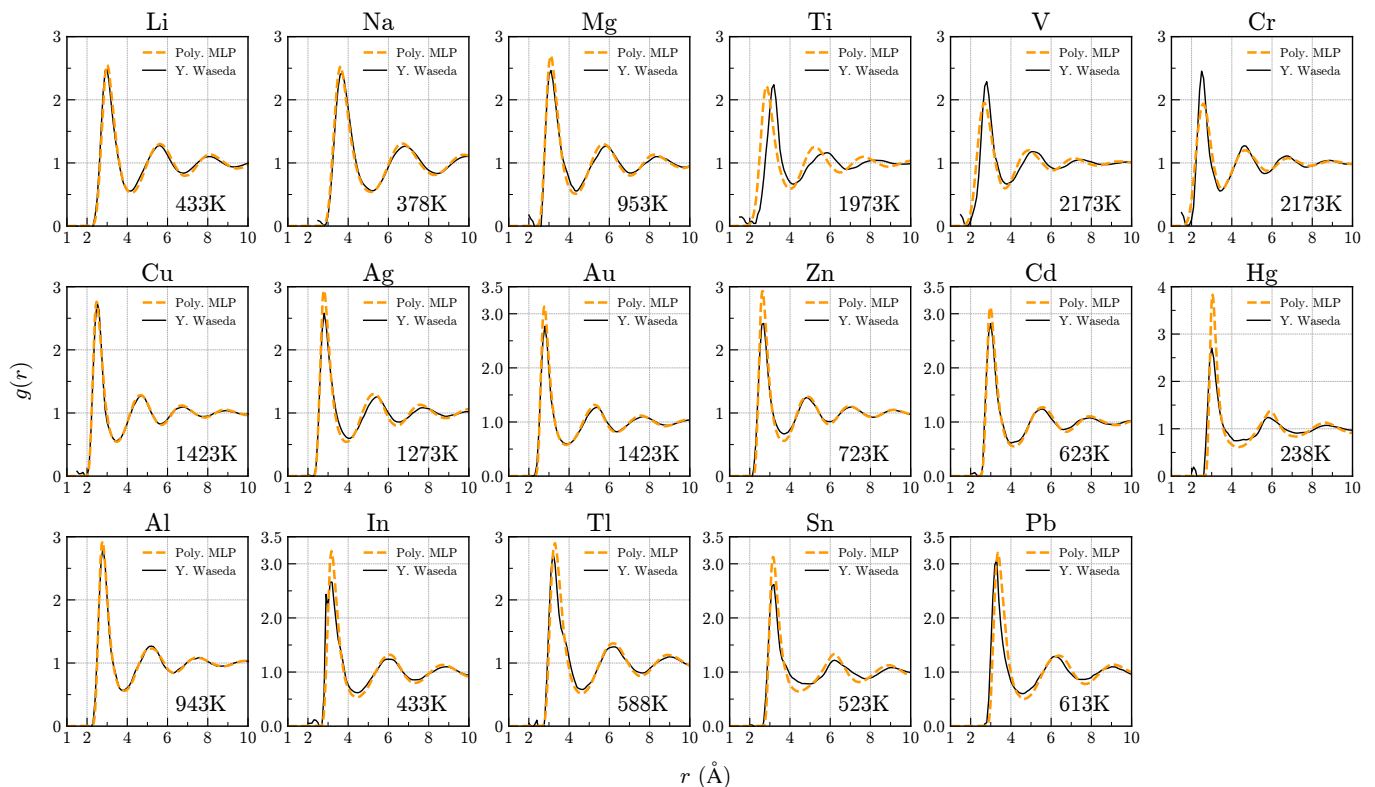


FIG. 27. RDFs obtained using polynomial MLPs along with experimental RDFs revealed by X-ray diffraction investigations [107].

Ge are consistent with the experimental structure factors. Although the polynomial MLP overestimates the peak intensities in elemental Bi, the structure factor calculated using the polynomial MLP is similar to the experimental one. The RDFs computed using the polynomial MLP and quadratic SNAP [72] are similar to the experimental RDFs in elemental Si. However, they slightly overestimate the interatomic distances in the experiments. In elemental Ga, the RDF obtained using the polynomial MLP agrees well with the experimental RDFs. In elemental Ge, the first peak position and the RDF at distances larger than 5 Å are consistent with the experimental ones. In contrast, the second peak in the experiments is not clearly observed in the RDF for the polynomial MLP. The second peak is recognized in the RDF for the quadratic SNAP [72], while its position is different from the experimental ones. In elemental Bi, the RDF computed using the polynomial MLP is similar to but slightly different from the experimental RDFs in terms of peak intensity. Thus, the polynomial MLPs can derive the RDFs close to the experimental RDFs within the range of deviations included in the experimental observations.

## 2. Other systems

Figure 26 shows the structure factor profiles revealed by X-ray diffraction investigations in the other elemen-

tal systems at temperatures close to the melting temperatures [107, 108]. However, no experimental structure factors are available for elemental Be. Figure 26 also shows the structure factors computed using the polynomial MLPs. The computational procedure is the same as explained in Appendix B 1. In elemental Li, Na, Cu, Cd, and Al, the structure factor profiles calculated using the polynomial MLPs agree with the experimental ones. In elemental Mg, Ag, Au, Zn, Hg, In, Tl, Sn, and Pb, the first peak intensities of the experimental and computational structure factor profiles are slightly different. However, the polynomial MLPs yield structural factor profiles that are almost the same as the experimental ones. In elemental V and Cr, the structure factors at wave numbers larger than  $4 \text{ \AA}^{-1}$  slightly differ from the experimental ones. In elemental Ti, the structure factor profile of the polynomial MLP is different from the experimental one investigated by Waseda [107]. However, it is consistent with the experimental one later investigated by Lee *et al.* [108].

Figure 27 shows the RDFs revealed by X-ray diffraction investigations in the 17 elemental systems at temperatures close to the melting temperatures [107]. The RDFs computed using the polynomial MLPs are also shown. The computational procedure is the same as described in Appendix B 1. In elemental Li, Na, Mg, Cu, Au, Cd, Al, and Tl, the RDFs computed using the polynomial MLPs are consistent with the experimental

RDFs. In elemental Cr, Zn, and In, the RDFs calculated using the polynomial MLPs are similar to the experimental RDFs, while the first peak intensities of the RDFs differ from those of the experimental RDFs. The interatomic distances and peak intensities in elemental V, Ag, Hg, Sn, and Pb are slightly different from the experimental ones. In elemental Ti, the polynomial MLP fails to

reproduce the experimental RDF [107]. However, this experimental RDF was obtained from the structure factor profile that is incompatible with the structure factor profile computed using the polynomial MLP, as shown in Fig. 26. On the other hand, the polynomial MLP has been shown to be capable of reconstructing the other experimental structure factor profile in elemental Ti [108].

- 
- [1] J. E. Lennard-Jones and S. Chapman, On the forces between atoms and ions, *Proc. R. Soc. London, Ser. A* **109**, 584 (1925).
- [2] M. S. Daw and M. I. Baskes, Embedded-atom method: Derivation and application to impurities, surfaces, and other defects in metals, *Phys. Rev. B* **29**, 6443 (1984).
- [3] F. H. Stillinger and T. A. Weber, Computer simulation of local order in condensed phases of silicon, *Phys. Rev. B* **31**, 5262 (1985).
- [4] M. I. Mendeleev, S. Han, D. J. Srolovitz, G. J. Ackland, D. Y. Sun, and M. Asta, Development of new interatomic potentials appropriate for crystalline and liquid iron, *Philos. Mag.* **83**, 3977 (2003).
- [5] M. Mendeleev, M. Kramer, C. Becker, and M. Asta, Analysis of semi-empirical interatomic potentials appropriate for simulation of crystalline and liquid Al and Cu, *Philos. Mag.* **88**, 1723 (2008).
- [6] J. Q. Broughton and X. P. Li, Phase diagram of silicon by molecular dynamics, *Phys. Rev. B* **35**, 9120 (1987).
- [7] S. Sastry and C. Austen Angell, Liquid-liquid phase transition in supercooled silicon, *Nat. Mater.* **2**, 739 (2003).
- [8] G. Kresse and J. Hafner, Ab initio molecular dynamics for liquid metals, *Phys. Rev. B* **47**, 558 (1993).
- [9] D. Marx and J. Hutter, *Ab initio Molecular Dynamics: Basic Theory and Advanced Methods* (Cambridge University Press, Cambridge, 2009).
- [10] S. Lorenz, A. Groß, and M. Scheffler, Representing high-dimensional potential-energy surfaces for reactions at surfaces by neural networks, *Chem. Phys. Lett.* **395**, 210 (2004).
- [11] J. Behler and M. Parrinello, Generalized neural-network representation of high-dimensional potential-energy surfaces, *Phys. Rev. Lett.* **98**, 146401 (2007).
- [12] A. P. Bartók, M. C. Payne, R. Kondor, and G. Csányi, Gaussian approximation potentials: The accuracy of quantum mechanics, without the electrons, *Phys. Rev. Lett.* **104**, 136403 (2010).
- [13] J. Behler, Atom-centered symmetry functions for constructing high-dimensional neural network potentials, *J. Chem. Phys.* **134**, 074106 (2011).
- [14] J. Han, L. Zhang, R. Car, and E. Weinan, Deep potential: A general representation of a many-body potential energy surface, *Commun. Comput. Phys.* **23**, 629 (2018).
- [15] N. Artrith and A. Urban, An implementation of artificial neural-network potentials for atomistic materials simulations: performance for TiO<sub>2</sub>, *Comput. Mater. Sci.* **114**, 135 (2016).
- [16] N. Artrith, A. Urban, and G. Ceder, Efficient and accurate machine-learning interpolation of atomic energies in compositions with many species, *Phys. Rev. B* **96**, 014112 (2017).
- [17] W. J. Szlachta, A. P. Bartók, and G. Csányi, Accuracy and transferability of gaussian approximation potential models for tungsten, *Phys. Rev. B* **90**, 104108 (2014).
- [18] A. P. Bartók, J. Kermode, N. Bernstein, and G. Csányi, Machine learning a general-purpose interatomic potential for silicon, *Phys. Rev. X* **8**, 041048 (2018).
- [19] Z. Li, J. R. Kermode, and A. De Vita, Molecular dynamics with on-the-fly machine learning of quantum-mechanical forces, *Phys. Rev. Lett.* **114**, 096405 (2015).
- [20] A. Glielmo, P. Sollich, and A. De Vita, Accurate interatomic force fields via machine learning with covariant kernels, *Phys. Rev. B* **95**, 214302 (2017).
- [21] A. Seko, A. Takahashi, and I. Tanaka, Sparse representation for a potential energy surface, *Phys. Rev. B* **90**, 024101 (2014).
- [22] A. Seko, A. Takahashi, and I. Tanaka, First-principles interatomic potentials for ten elemental metals via compressed sensing, *Phys. Rev. B* **92**, 054113 (2015).
- [23] A. Takahashi, A. Seko, and I. Tanaka, Conceptual and practical bases for the high accuracy of machine learning interatomic potentials: Application to elemental titanium, *Phys. Rev. Mater.* **1**, 063801 (2017).
- [24] A. P. Thompson, L. P. Swiler, C. R. Trott, S. M. Foiles, and G. J. Tucker, Spectral neighbor analysis method for automated generation of quantum-accurate interatomic potentials, *J. Comput. Phys.* **285**, 316 (2015).
- [25] M. A. Wood and A. P. Thompson, Extending the accuracy of the SNAP interatomic potential form, *J. Chem. Phys.* **148**, 241721 (2018).
- [26] C. Chen, Z. Deng, R. Tran, H. Tang, I.-H. Chu, and S. P. Ong, Accurate force field for molybdenum by machine learning large materials data, *Phys. Rev. Mater.* **1**, 043603 (2017).
- [27] A. V. Shapeev, Moment tensor potentials: A class of systematically improvable interatomic potentials, *Multiscale Model. Simul.* **14**, 1153 (2016).
- [28] T. Mueller, A. Hernandez, and C. Wang, Machine learning for interatomic potential models, *J. Chem. Phys.* **152**, 050902 (2020).
- [29] R. Freitas and Y. Cao, Machine-learning potentials for crystal defects, *MRS Commun.* **10.1557/s43579-022-00221-5** (2022).
- [30] V. L. Deringer and G. Csányi, Machine learning based interatomic potential for amorphous carbon, *Phys. Rev. B* **95**, 094203 (2017).
- [31] B. Cheng, E. A. Engel, J. Behler, C. Dellago, and M. Ceriotti, Ab initio thermodynamics of liquid and solid water, *Proc. Natl. Acad. Sci. U.S.A.* **116**, 1110 (2019).
- [32] A. Seko, A. Togo, and I. Tanaka, Group-theoretical high-order rotational invariants for structural representations: Application to linearized machine learning in-

- teratomic potential, *Phys. Rev. B* **99**, 214108 (2019).
- [33] A. Seko, Machine learning potentials for multicomponent systems: The Ti-Al binary system, *Phys. Rev. B* **102**, 174104 (2020).
- [34] A. Seko, Tutorial: Systematic development of polynomial machine learning potentials for elemental and alloy systems, *J. Appl. Phys.* **133**, 011101 (2023).
- [35] A. Seko, Polynomial Machine Learning Potential Repository at Kyoto University, <https://sekocha.github.io>.
- [36] T. Nishiyama, A. Seko, and I. Tanaka, Application of machine learning potentials to predict grain boundary properties in fcc elemental metals, *Phys. Rev. Mater.* **4**, 123607 (2020).
- [37] S. Fujii and A. Seko, Structure and lattice thermal conductivity of grain boundaries in silicon by using machine learning potential and molecular dynamics, *Comput. Mater. Sci.* **204**, 111137 (2022).
- [38] D. C. Wallace, *Statistical Physics of Crystals and Liquids* (WORLD SCIENTIFIC, 2003).
- [39] H. Tanaka, Simple view of waterlike anomalies of atomic liquids with directional bonding, *Phys. Rev. B* **66**, 064202 (2002).
- [40] D. Dhabal, C. Chakravarty, V. Molinero, and H. K. Kashyap, Comparison of liquid-state anomalies in Stillinger-Weber models of water, silicon, and germanium, *J. Chem. Phys.* **145**, 214502 (2016).
- [41] M. El-Batanouny and F. Wooten, *Symmetry and Condensed Matter Physics: A Computational Approach* (Cambridge University Press, Cambridge, 2008).
- [42] R. Drautz, Atomic cluster expansion for accurate and transferable interatomic potentials, *Phys. Rev. B* **99**, 014104 (2019).
- [43] A. Seko, <https://github.com/sekocha/pyppolympl>.
- [44] G. Bergerhoff and I. D. Brown, in *Crystallographic Databases*, edited by F. H. Allen et al. (International Union of Crystallography, Chester, 1987).
- [45] P. E. Blöchl, Projector augmented-wave method, *Phys. Rev. B* **50**, 17953 (1994).
- [46] G. Kresse and D. Joubert, From ultrasoft pseudopotentials to the projector augmented-wave method, *Phys. Rev. B* **59**, 1758 (1999).
- [47] J. P. Perdew, K. Burke, and M. Ernzerhof, Generalized Gradient Approximation Made Simple, *Phys. Rev. Lett.* **77**, 3865 (1996).
- [48] G. Kresse and J. Furthmüller, Efficient iterative schemes for ab initio total-energy calculations using a plane-wave basis set, *Phys. Rev. B* **54**, 11169 (1996).
- [49] G. Kresse and J. Furthmüller, Efficiency of ab-initio total energy calculations for metals and semiconductors using a plane-wave basis set, *Comput. Mater. Sci.* **6**, 15 (1996).
- [50] E. B. Tadmor, R. S. Elliott, J. P. Sethna, R. E. Miller, and C. A. Becker, The potential of atomistic simulations and the knowledgebase of interatomic models., *JOM* **63**, 17 (2011).
- [51] C. A. Becker, F. Tavazza, Z. T. Trautt, and R. A. Buarque de Macedo, Considerations for choosing and using force fields and interatomic potentials in materials science and engineering, *Curr. Opin. Solid State Mater. Sci.* **17**, 277 (2013), frontiers in Methods for Materials Simulations.
- [52] S. Nosé, A unified formulation of the constant temperature molecular dynamics methods, *J. Chem. Phys.* **81**, 511 (1984).
- [53] W. G. Hoover, Canonical dynamics: Equilibrium phase-space distributions, *Phys. Rev. A* **31**, 1695 (1985).
- [54] A. P. Thompson *et al.*, LAMMPS - a flexible simulation tool for particle-based materials modeling at the atomic, meso, and continuum scales, *Comput. Phys. Commun.* **271**, 108171 (2022).
- [55] A. F. Crawley, Densities of Liquid Metals and Alloys, *Int. Metall. Rev.* **19**, 32 (1974).
- [56] G. Kresse and J. Hafner, Ab initio simulation of the metal/nonmetal transition in expanded fluid mercury, *Phys. Rev. B* **55**, 7539 (1997).
- [57] M. P. Allen and D. J. Tildesley, *Computer Simulation of Liquids* (Oxford University Press, Oxford, 2017).
- [58] M. E. Tuckerman, *Statistical Mechanics Theory and Molecular Simulation* (Oxford Graduate Texts, Oxford, 2010).
- [59] I. Štich, R. Car, and M. Parrinello, Bonding and disorder in liquid silicon, *Phys. Rev. Lett.* **63**, 2240 (1989).
- [60] T. H. Kim and K. F. Kelton, Structural study of supercooled liquid transition metals, *J. Chem. Phys.* **126**, 054513 (2007).
- [61] S. Munetoh, T. Motooka, K. Moriguchi, and A. Shintani, Interatomic potential for Si-O systems using Tersoff parameterization, *Comput. Mater. Sci.* **39**, 334 (2007).
- [62] P. J. Steinhardt, D. R. Nelson, and M. Ronchetti, Bond-orientational order in liquids and glasses, *Phys. Rev. B* **28**, 784 (1983).
- [63] W. Lechner and C. Dellago, Accurate determination of crystal structures based on averaged local bond order parameters, *J. Chem. Phys.* **129**, 114707 (2008).
- [64] L.-Y. Chen, P.-H. Tang, and T.-M. Wu, Analysis of local bond-orientational order for liquid gallium at ambient pressure: Two types of cluster structures, *J. Chem. Phys.* **145**, 024506 (2016).
- [65] S. Winczewski, J. Dziejczak, and J. Rybicki, In-depth characterization of icosahedral ordering in liquid copper, *Comput. Mater. Sci.* **166**, 57 (2019).
- [66] W. M. Haynes, *CRC Handbook of Chemistry and Physics*, 92nd ed. (CRC Press, Boca Raton, FL, 2012).
- [67] S. Makridakis, Accuracy measures: theoretical and practical concerns, *Int. J. Forecast.* **9**, 527 (1993).
- [68] P. Erhart and K. Albe, Analytical potential for atomistic simulations of silicon, carbon, and silicon carbide, *Phys. Rev. B* **71**, 035211 (2005).
- [69] S. J. Mahdizadeh and G. Akhlagi, Optimized Tersoff empirical potential for germanene, *J. Mol. Graph. Model.* **72**, 1 (2017).
- [70] Y. A. Du, T. J. Lenosky, R. G. Hennig, S. Goedecker, and J. W. Wilkins, Energy landscape of silicon tetra-interstitials using an optimized classical potential, *Phys. Status Solidi B* **248**, 2050 (2011).
- [71] E. H. Kim, Y.-H. Shin, and B.-J. Lee, A modified embedded-atom method interatomic potential for Germanium, *Calphad* **32**, 34 (2008).
- [72] Y. Zuo *et al.*, Performance and Cost Assessment of Machine Learning Interatomic Potentials, *J. Phys. Chem. A* **124**, 731 (2020), pMID: 31916773.
- [73] Y.-M. Kim, I.-H. Jung, and B.-J. Lee, Atomistic modeling of pure Li and Mg-Li system, *Modell. Simul. Mater. Sci. Eng.* **20**, 035005 (2012).
- [74] A. Agrawal, R. Mishra, L. Ward, K. M. Flores, and W. Windl, An embedded atom method potential of

- beryllium, *Modell. Simul. Mater. Sci. Eng.* **21**, 085001 (2013).
- [75] J. Wei, W. Zhou, S. Li, P. Shen, S. Ren, A. Hu, and W. Zhou, Modified Embedded Atom Method Potential for Modeling the Thermodynamic Properties of High Thermal Conductivity Beryllium Oxide, *ACS Omega* **4**, 6339 (2019), pMID: 31459774.
- [76] A. Nichol and G. J. Ackland, Property trends in simple metals: An empirical potential approach, *Phys. Rev. B* **93**, 184101 (2016).
- [77] Y. Kim, W.-S. Ko, and B.-J. Lee, Second nearest-neighbor modified embedded atom method interatomic potentials for the Na unary and Na-Sn binary systems, *Comput. Mater. Sci.* **185**, 109953 (2020).
- [78] D. Y. Sun, M. I. Mendeleev, C. A. Becker, K. Kudin, T. Haxhimali, M. Asta, J. J. Hoyt, A. Karma, and D. J. Srolovitz, Crystal-melt interfacial free energies in hcp metals: A molecular dynamics study of Mg, *Phys. Rev. B* **73**, 024116 (2006).
- [79] S. R. Wilson and M. I. Mendeleev, A unified relation for the solid-liquid interface free energy of pure FCC, BCC, and HCP metals, *J. Chem. Phys.* **144**, 144707 (2016).
- [80] X. W. Zhou, R. A. Johnson, and H. N. G. Wadley, Misfit-energy-increasing dislocations in vapor-deposited CoFe/NiFe multilayers, *Phys. Rev. B* **69**, 144113 (2004).
- [81] R. G. Hennig, T. J. Lenosky, D. R. Trinkle, S. P. Rudin, and J. W. Wilkins, Classical potential describes martensitic phase transformations between the  $\alpha$ ,  $\beta$ , and  $\omega$  titanium phases, *Phys. Rev. B* **78**, 054121 (2008).
- [82] P. M. Derlet, D. Nguyen-Manh, and S. L. Dudarev, Multiscale modeling of crowdion and vacancy defects in body-centered-cubic transition metals, *Phys. Rev. B* **76**, 054107 (2007).
- [83] B. J. Lee, M. I. Baskes, H. Kim, and Y. K. Cho, Second nearest-neighbor modified embedded atom method potentials for bcc transition metals, *Phys. Rev. B* **64**, 184102 (2001).
- [84] G. Bonny, N. Castin, and D. Terentyev, Interatomic potential for studying ageing under irradiation in stainless steels: the FeNiCr model alloy, *Modell. Simul. Mater. Sci. Eng.* **21**, 085004 (2013).
- [85] S. A. Etesami and E. Asadi, Molecular dynamics for near melting temperatures simulations of metals using modified embedded-atom method, *J. Phys. Chem. Solids* **112**, 61 (2018).
- [86] P. L. Williams, Y. Mishin, and J. C. Hamilton, An embedded-atom potential for the Cu-Ag system, *Modell. Simul. Mater. Sci. Eng.* **14**, 817 (2006).
- [87] V. Zhakhovskii, N. Inogamov, Y. Petrov, S. Ashitkov, and K. Nishihara, Molecular dynamics simulation of femtosecond ablation and spallation with different interatomic potentials, *Appl. Surf. Sci.* **255**, 9592 (2009).
- [88] G. P. P. Pun, EAM potential (LAMMPS cubic hermite tabulation) for Au developed by Pun (2017) v000, OpenKIM, <https://doi.org/10.25950/b433cd2b> (2018).
- [89] J. Lennard-Jones, Efficient 'universal' shifted Lennard-Jones model for all KIM API supported species developed by Elliott and Akerson (2015) v003, OpenKIM, <https://doi.org/10.25950/962b4967> (2018).
- [90] H.-S. Jang, K.-M. Kim, and B.-J. Lee, Modified embedded-atom method interatomic potentials for pure Zn and Mg-Zn binary system, *Calphad* **60**, 200 (2018).
- [91] P. Brommer, F. Gähler, and M. Mihalkovič, Ordering and correlation of cluster orientations in CaCd<sub>6</sub>, *Philos. Mag.* **87**, 2671 (2007).
- [92] D. K. Ward, X. W. Zhou, B. M. Wong, F. P. Doty, and J. A. Zimmerman, Analytical bond-order potential for the cadmium telluride binary system, *Phys. Rev. B* **85**, 115206 (2012).
- [93] X. W. Zhou, D. K. Ward, J. E. Martin, F. B. van Swol, J. L. Cruz-Campa, and D. Zubia, Stillinger-Weber potential for the II-VI elements Zn-Cd-Hg-S-Se-Te, *Phys. Rev. B* **88**, 085309 (2013).
- [94] M. Pascuet and J. Fernández, Atomic interaction of the MEAM type for the study of intermetallics in the Al-U alloy, *J. Nucl. Mater.* **467**, 229 (2015).
- [95] E. C. Do, Y.-H. Shin, and B.-J. Lee, Atomistic modeling of III-V nitrides: modified embedded-atom method interatomic potentials for GaN, InN, and Ga<sub>1-x</sub>In<sub>x</sub>N, *J. Phys.: Condens. Matter* **21**, 325801 (2009).
- [96] D. A. Murdick, X. W. Zhou, H. N. G. Wadley, D. Nguyen-Manh, R. Drautz, and D. G. Pettifor, Analytic bond-order potential for the gallium arsenide system, *Phys. Rev. B* **73**, 045206 (2006).
- [97] E. C. Do, Y.-H. Shin, and B.-J. Lee, A modified embedded-atom method interatomic potential for indium, *Calphad* **32**, 82 (2008).
- [98] J. R. Vella, M. Chen, F. H. Stillinger, E. A. Carter, P. G. Debenedetti, and A. Z. Panagiotopoulos, Structural and dynamic properties of liquid tin from a new modified embedded-atom method force field, *Phys. Rev. B* **95**, 064202 (2017).
- [99] A. Landa, P. Wynblatt, D. Siegel, J. Adams, O. Mryasov, and X.-Y. Liu, Development of glue-type potentials for the Al-Pb system: phase diagram calculation, *Acta Mater.* **48**, 1753 (2000).
- [100] H. Zhou, D. E. Dickel, M. I. Baskes, S. Mun, and M. A. Zaeem, A modified embedded-atom method interatomic potential for bismuth, *Modell. Simul. Mater. Sci. Eng.* **29**, 065008 (2021).
- [101] J. P. Gabathuler and S. Steeb, Über die Struktur von Si-, Ge-, Sn- und Pb-Schmelzen / Structure of Si-, Ge-, Sn-, and Pb-melts, *Z. Naturforsch. A* **34**, 1314 (1979).
- [102] Y. Waseda and K. Suzuki, Structure of molten silicon and germanium by X-ray diffraction, *Z. Phys. B: Condens. Matter* **20**, 339 (1975).
- [103] A. H. Narten, Liquid Gallium: Comparison of X-Ray and Neutron-Diffraction Data, *J. Chem. Phys.* **56**, 1185 (2003).
- [104] M. C. Bellissent-Funel, P. Chieux, D. Levesque, and J. J. Weis, Structure factor and effective two-body potential for liquid gallium, *Phys. Rev. A* **39**, 6310 (1989).
- [105] E. N. Caspi, Y. Greenberg, E. Yahel, B. Beuneu, and G. Makov, What is the structure of liquid Bismuth?, *J. Phys. Conf. Ser.* **340**, 012079 (2012).
- [106] Y. Waseda and K. Suzuki, Structure factor and atomic distribution in liquid metals by X-ray diffraction, *Phys. Status Solidi B* **49**, 339 (1972).
- [107] Y. Waseda, *The Structure of Non-crystalline Materials: Liquids and Amorphous Solids*, Advanced Book Program (McGraw-Hill International Book Company, 1980).
- [108] G. W. Lee, A. K. Gangopadhyay, K. F. Kelton, R. W. Hyers, T. J. Rathz, J. R. Rogers, and D. S. Robinson, Difference in Icosahedral Short-Range Order in Early

- and Late Transition Metal Liquids, *Phys. Rev. Lett.* **93**, 037802 (2004).
- [109] B. G. del Rio and L. E. González, Orbital free ab initio simulations of liquid alkaline earth metals: from pseudopotential construction to structural and dynamic properties, *J. Phys. Condens. Matter* **26**, 465102 (2014).
- [110] B. Lee and G. W. Lee, A liquid-liquid transition can exist in monatomic transition metals with a positive melting slope, *Sci. Rep.* **6**, 35564 (2016).
- [111] T. T. Debela, X. D. Wang, Q. P. Cao, D. X. Zhang, and J. Z. Jiang, The crystallization process of liquid vanadium studied by ab initio molecular dynamics, *J. Phys.: Condens. Matter* **26**, 155101 (2014).
- [112] P. Ganesh and M. Widom, Signature of nearly icosahedral structures in liquid and supercooled liquid copper, *Phys. Rev. B* **74**, 134205 (2006).
- [113] G. Bhuiyan, L. González, and D. González, Orbital free ab initio molecular dynamics simulation study of some static and dynamic properties of liquid noble metals, *Condens. Matter Phys.* **15**, 33604 (2012).
- [114] M. R. Molla, A. Ziauddin Ahmed, H. Sarker, G. Bhuiyan, M. Amin, L. González, and D. González, Static and dynamic properties of liquid Zn, Cd and Hg divalent metals: An orbital free ab initio molecular dynamics study, *J. Non-Cryst. Solids* **406**, 45 (2014).
- [115] N. Jakse and A. Pasturel, Liquid Aluminum: Atomic diffusion and viscosity from ab initio molecular dynamics, *Sci. Rep.* **3**, 3135 (2013).
- [116] J. Yang, J. S. Tse, and T. Iitaka, First-principles study of liquid gallium at ambient and high pressure, *J. Chem. Phys.* **135**, 044507 (2011).
- [117] A. V. Mokshin, R. M. Khusnutdinoff, B. N. Galimzyanov, and V. V. Brazhkin, Extended short-range order determines the overall structure of liquid gallium, *Phys. Chem. Chem. Phys.* **22**, 4122 (2020).
- [118] G. Kresse, Ab initio molecular dynamics: recent progresses and limitations, *J. Non-Cryst. Solids* **312-314**, 52 (2002).
- [119] R. C. Remsing, M. L. Klein, and J. Sun, Dependence of the structure and dynamics of liquid silicon on the choice of density functional approximation, *Phys. Rev. B* **96**, 024203 (2017).
- [120] M. M. G. Alemany, R. C. Longo, L. J. Gallego, D. J. González, L. E. González, M. L. Tiago, and J. R. CheLIKowsky, Ab initio molecular dynamics simulations of the static, dynamic, and electronic properties of liquid Pb using real-space pseudopotentials, *Phys. Rev. B* **76**, 214203 (2007).
- [121] B. Galimzyanov, A. Tsygankov, A. Suslov, V. Lad'yanov, and A. Mokshin, Quasi-stable structures in equilibrium dense bismuth melt: Experimental and first principles theoretical studies, *Scripta Mater.* **235**, 115618 (2023).

## Supplemental Material: Predictive power of polynomial machine learning potentials for liquid states in 22 elemental systems

### 1. Absolute prediction errors for 86 prototype structures

Figures S28, S29, and S30 show the absolute prediction errors of the cohesive energy for 86 prototype structures in 22 elemental systems, i.e., Li, Be, Na, Mg, Al, Si, Ti, V, Cr, Cu, Zn, Ga, Ge, Ag, Cd, In, Sn, Au, Hg, Tl, Pb, and Bi. The polynomial MLP exhibits small errors for almost all prototype structures. These results indicate that the polynomial MLP is accurate for many typical structures containing diverse neighborhood environments and coordination numbers.

### 2. The RDFs calculated using all Pareto-optimal polynomial MLPs

Figures S31, S32, and S33 exhibit the RDFs calculated using all Pareto-optimal polynomial MLPs at a temperature above and closest to the melting temperature among our temperature settings in elemental Li, Be, Na, Mg, Al, Si, Ti, V, Cr, Cu, Zn, Ga, Ge, Ag, Cd, In, Sn, Au, Hg, Tl, Pb, and Bi. Most of the polynomial MLPs yield accurate RDFs, except for simplistic polynomial MLPs, and the predictive power for liquid structures is independent of the selection of the polynomial MLP.

### 3. Test DFT calculations using different PAW potentials

We performed AIMD simulations and calculated RDFs using PAW potentials that differ from those applied in the main text for elemental Ti and V. In these PAW potentials,  $3s$  and  $3p$  semi-core electrons are regarded as valence states. We followed the same computational procedures described in Sec. II B, except that we increased the cutoff energy to 500 eV because these PAW potentials require a higher cutoff energy for accurate DFT calculations. Figure S34 shows the RDFs obtained from DFT calculations at 1950 and 2200 K in elemental Ti and V, respectively. Although the peak intensities of the RDFs computed using the two kinds of PAW potentials differ slightly in both systems, there are no significant differences.

#### 4. Comparison with RDFs obtained from DFT calculations in the literature

Here, we compare the RDFs computed using the polynomial MLPs with those obtained from DFT calculations reported in the literature [56, 109–121]. The RDFs calculated using the polynomial MLPs are obtained through the procedure described in Appendix A. Figure S35 shows the comparison between the RDFs obtained from the polynomial MLP and those reported in the literature.

In many systems, the RDFs calculated using the polynomial MLPs are comparable to those calculated using DFT calculations reported in the literature. However, in some systems, there are slight differences in the peak intensities and interatomic distances obtained using the polynomial MLPs as compared to the DFT calculations reported in the literature. Note that the computational procedure and conditions for the DFT calculations in the literature, such as the exchange-correlation functional type, the ensemble type, the number of atoms in the simulation box, and the number of steps, are often different from those used in this study.

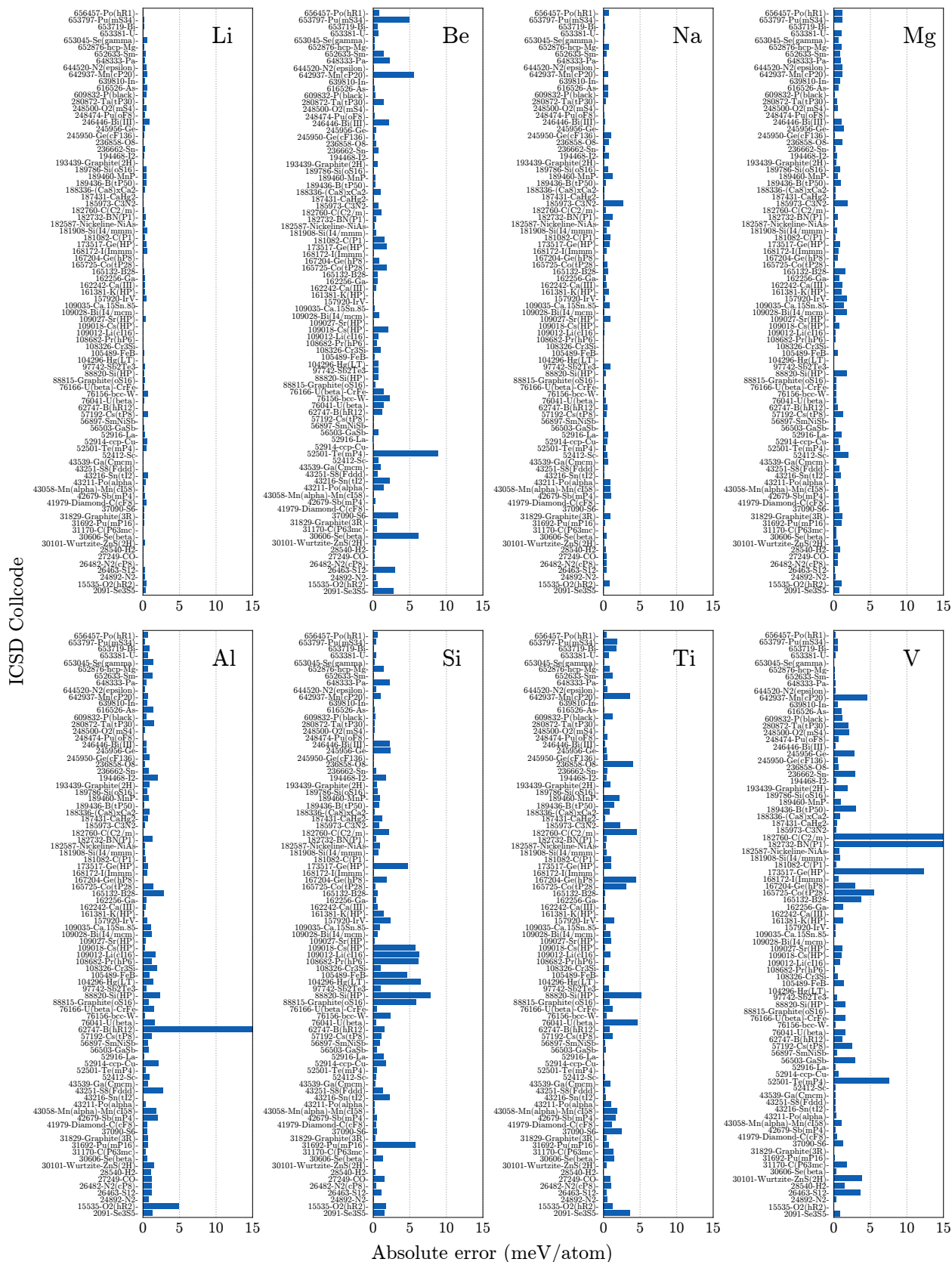


FIG. S28. Absolute prediction errors of the cohesive energy for 86 prototype structures in elemental Li, Be, Na, Mg, Al, Si, Ti, and V.

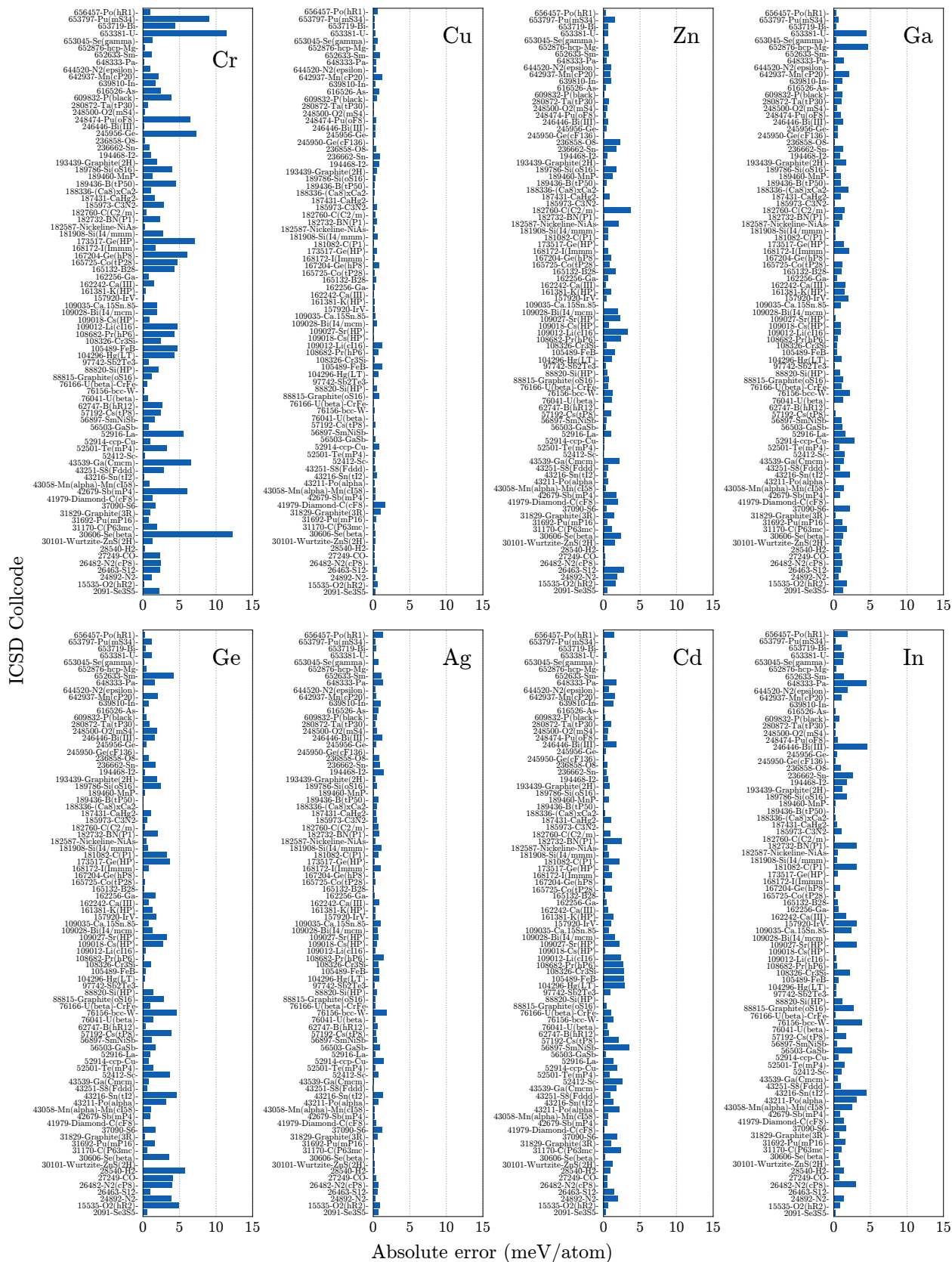


FIG. S29. Absolute prediction errors of the cohesive energy for 86 prototype structures in elemental Cr, Cu, Zn, Ga, Ge, Ag, Cd, and In.

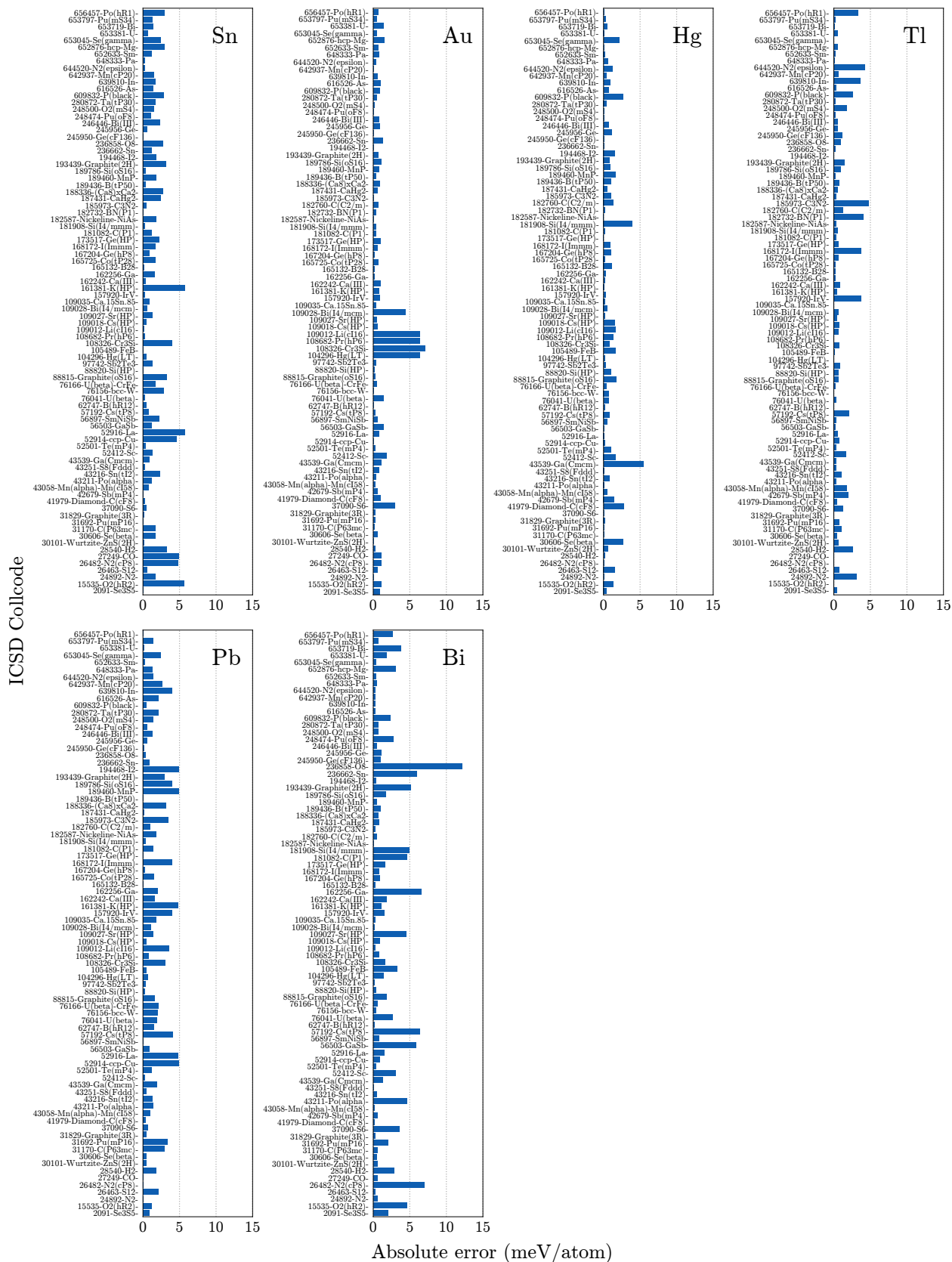


FIG. S30. Absolute prediction errors of the cohesive energy for 86 prototype structures in elemental Sn, Au, Hg, Tl, Pb, and Bi.

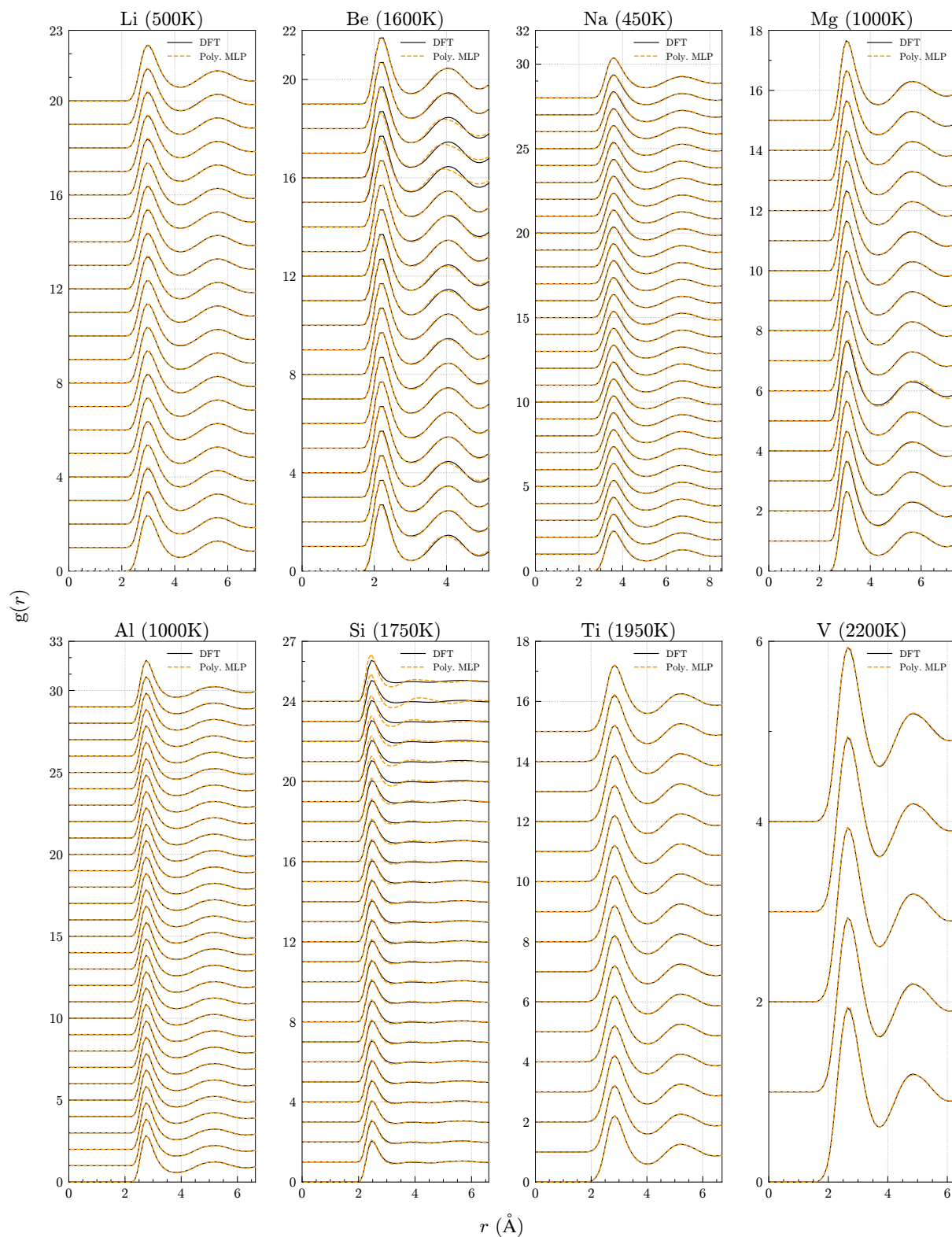


FIG. S31. RDFs calculated using all the Pareto-optimal polynomial MLPs at a temperature above and closest to the melting temperature among our temperature settings in elemental Li, Be, Na, Mg, Al, Si, Ti, and V. The RDFs calculated using each polynomial MLP are shifted upwards by the amount of 1.0. The RDFs are shown from top to bottom in the ascending order of the computational cost. In the legend, Poly. MLP stands for polynomial MLP.

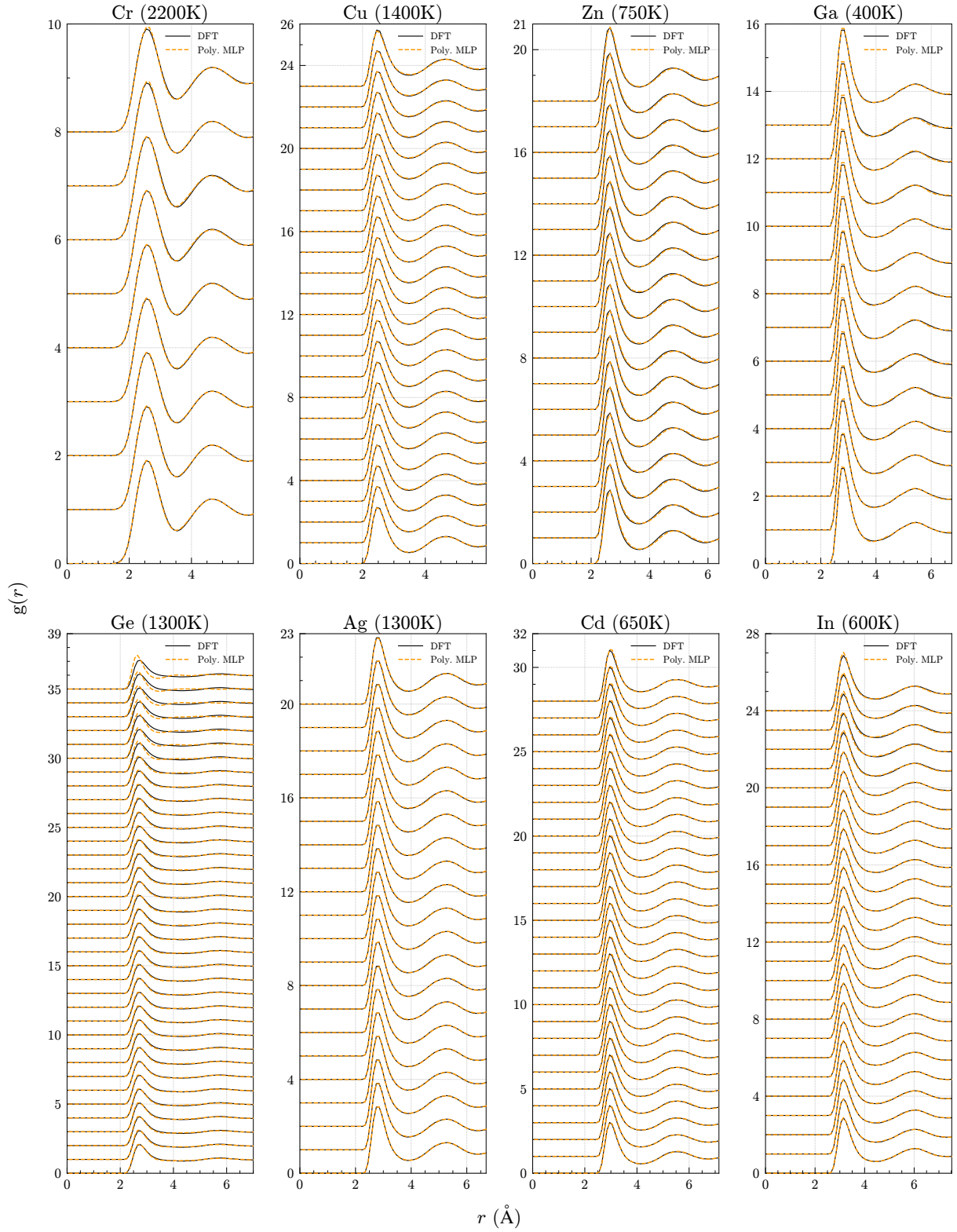


FIG. S32. RDFs calculated using all the Pareto-optimal polynomial MLPs at a temperature above and closest to the melting temperature among our temperature settings in elemental Cr, Cu, Zn, Ga, Ge, Ag, Cd, and In. The RDFs calculated using each MLP are shifted upwards by the amount of 1.0. The RDFs are shown from top to bottom in the ascending order of the computational cost. In the legend, Poly. MLP stands for polynomial MLP.

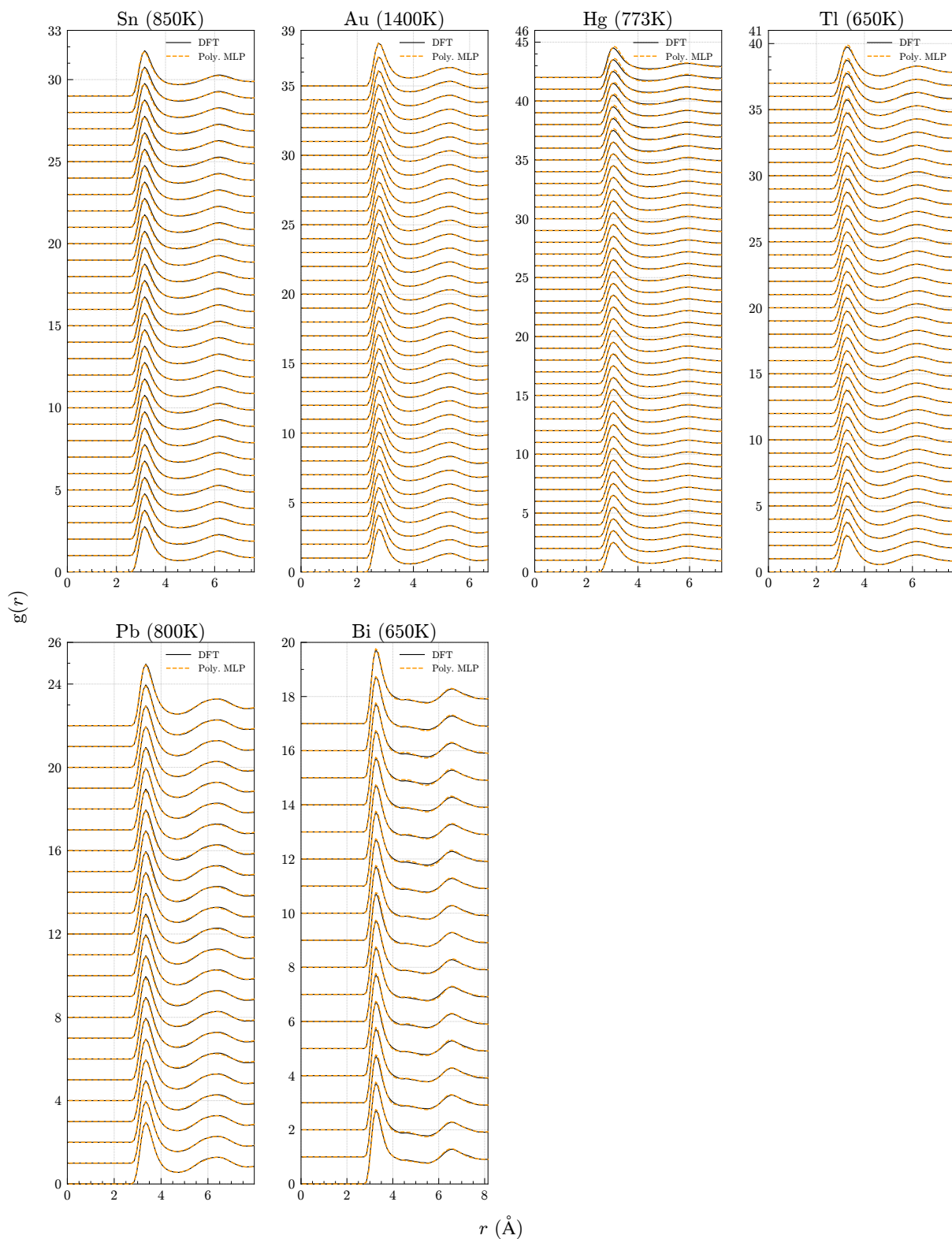


FIG. S33. RDFs calculated using all the Pareto-optimal polynomial MLPs at a temperature above and closest to the melting temperature among our temperature settings in elemental Sn, Au, Hg, Tl, Pb, and Bi. The RDFs calculated using each MLP are shifted upwards by the amount of 1.0. The RDFs are shown from top to bottom in the ascending order of the computational cost. In the legend, Poly. MLP stands for polynomial MLP.

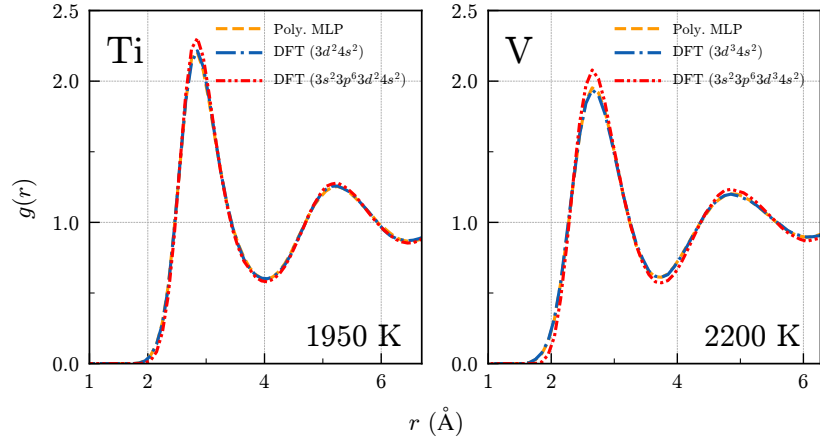


FIG. S34. RDFs obtained from DFT calculations with the two kinds of PAW potentials in elemental Ti and V.

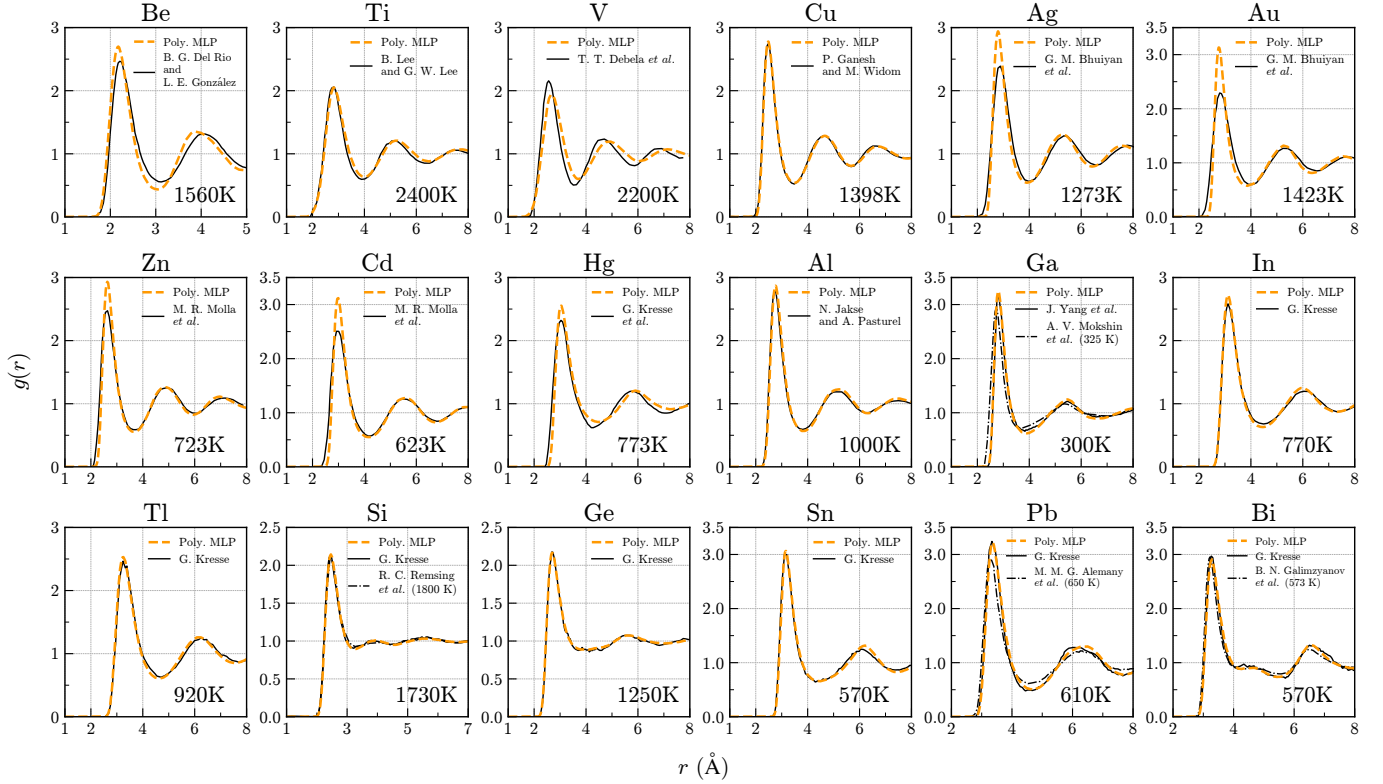


FIG. S35. RDFs obtained from the MD simulations using the polynomial MLP in 18 elemental systems, along with RDFs obtained from other DFT calculations [56, 109–121]. (Be [109], Ti [110], V [111], Cu [112], Ag [113], Au [113], Zn [114], Cd [114], Hg [56], Al [115], Ga [116, 117], In [118], Tl [118], Si [118, 119], Ge [118], Sn [118], Pb [118, 120], Bi [118, 121]).